

SPIN IN DARK MATTER PROBLEM

V. A. Bednyakov*

Joint Institute for Nuclear Research, Dubna

The Weakly Interacting Massive Particles (WIMPs) are among the main candidates for the relic Dark Matter (DM). The idea of the direct DM detection relies on elastic Spin-Dependent (SD) and Spin-Independent (SI) interaction of WIMPs with target nuclei. In this review formulas for the DM event rate calculations are collected. The importance of the SD WIMP–nucleus interaction for reliable DM detection is argued and the relevant to DM search spin nuclear structure functions are discussed. The effective low-energy minimal supersymmetric standard model (MSSM) is used for calculation of the DM cross sections, provided the lightest neutralino is the WIMP. It is shown that the absolute lower bound for the rate of direct DM detection is due to the SD WIMP–nucleon interaction, and a new-generation experiment aimed at *detecting* DM with sensitivity higher than 10^{-5} event/(kg · day) should have a nonzero-spin target to avoid missing of the DM signal. The mixed spin–scalar couplings approach is argued. Prospects of DM experiments with high-spin Ge-73 are discussed in the mixed coupling scheme. The DAMA experiment has claimed observation of the WIMPs due to the annual signal modulation. Some important consequences of the DAMA claim for the other DM searches as well as for collider physics are considered.

Как известно, массивные слабодействующие частицы (WIMPs) являются одними из основных кандидатов на роль реликтовой темной материи (DM). Идея их прямого детектирования базируется на спин-зависимом (SD) и спин-независимом (SI) характере их упругого взаимодействия с ядрами мишеней расположенных на Земле детекторов. В данном обзоре собраны все необходимые формулы и соотношения для вычисления ожидаемой скорости счета событий прямого детектирования частиц DM. Кроме этого, обсуждается важность SD WIMP-ядерного взаимодействия для детектирования темной материи, а также дается обзор всех имеющих отношение к проблеме DM спиновых структурных функций ядра. Для вычисления сечений взаимодействия легчайших нейтралино (в роли частиц DM) с нуклонами используется эффективная низкоэнергетическая версия минимального суперсимметричного расширения стандартной модели (MSSM). Показано, что наличие нижней границы для скорости счета событий прямого детектирования DM обусловлено, главным образом, SD WIMP-нуклонным взаимодействием. По этой причине, чтобы не пропустить DM-сигнал, эксперименты, нацеленные на детектирование частиц DM с рекордной чувствительностью на уровне 10^{-5} событий/(кг · сут), должны обязательно иметь в качестве мишени ядра с отличными от нуля спинами. В обзоре также аргументируется предпочтительное использование нового подхода к анализу DM-данных, учитывающего ненулевые значения скалярной и спиновой констант связи WIMP с нуклонами. В рамках этого подхода обсуждаются перспективы экспериментов с высокоспиновым ядром Ge-73. Как известно, пока только в эксперименте DAMA удалось получить первые свидетельства существования частиц DM путем измерения ожидаемой годовой модуляции сигнала. В обзоре рассмотрены некоторые важные следствия этого наблюдения, которые могут быть проверены как в других DM-экспериментах, так и на коллайдерах при сверхвысоких энергиях.

PACS: 95.35.+d, 12.60.Jv, 14.80.Ly

*E-mail: Vadim.Bednyakov@jinr.ru

INTRODUCTION

By definition, galactic Dark Matter (DM) does not emit detectable amounts of electromagnetic radiation and only gravitationally affects other, visible, celestial bodies. The best (and historically one of the first) evidence of this kind comes from the study of galactic rotation curves, when one measures the velocity with which globular stellar clusters, gas clouds, or dwarf galaxies orbit around their centers. If the mass of these galaxies were concentrated in their visible parts, the orbital velocity at large radii r should decrease as $1/\sqrt{r}$ (Fig. 1). Instead, it remains approximately constant to the largest radius where it can be measured. This implies that the total mass $M(r)$ felt by an object at a radius r must increase linearly with r (Fig. 2). Studies of this type imply that 90% or more of the mass of large galaxies is dark.

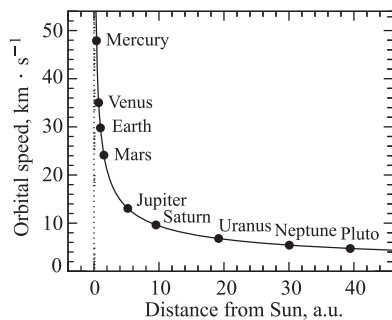


Fig. 1. Rotation curve of the solar system which falls off as $v = \sqrt{G_N M/r}$ in accordance with Kepler's law. a.u. is the Earth-Sun distance of $1.5 \cdot 10^{13}$ cm

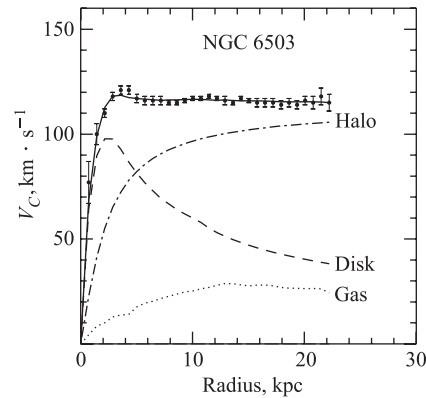


Fig. 2. Rotation curve of the spiral galaxy NGC 6503 as established from radio observations of hydrogen gas in the disk

The mass density averaged over the entire Universe is usually expressed in units of critical density $\rho_c \approx 10^{-29}$ g/cm³, the dimensionless ratio $\Omega \equiv \rho/\rho_c = 1$ corresponds to a flat Universe. Analyses of galactic rotation curves imply $\Omega \geq 0.1$. Studies of clusters and superclusters of galaxies through gravitational lensing or through measurements of their X-ray temperature, as well as studies of the large-scale streaming of galaxies favor larger values of the total mass density of the Universe $\Omega \geq 0.3$ (see, for example, [3]). Finally, naturalness arguments and inflationary models prefer $\Omega = 1.0$ to a high accuracy. The requirement that the Universe be at least 10 billion years old implies $\Omega h^2 \leq 1$, where h is the present Hubble parameter in units of 100 km/(s · Mpc). The total density of luminous matter only amounts to less than 1% of the critical density. Analyses

of Big Bang nucleosynthesis determine the total baryonic density to lie in the range $0.01 \leq \Omega_{\text{bar}} h^2 \leq 0.015$. The upper bound implies $\Omega_{\text{bar}} \leq 0.06$, in obvious conflict with the lower bound $\Omega \geq 0.3$. Most dark matter must therefore be nonbaryonic. Some sort of «new physics» is required to describe this exotic matter, beyond the particles described by the Standard Model of particle physics.

Exciting evidence for a flat and accelerating Universe was obtained [4, 5]. The position of the first acoustic peak (in Fig. 3) of the angular power spectrum strongly suggests a flat universe with density parameter $\Omega_0 = 1$ while the shape of the peak is consistent with the density perturbations predicted by models of inflation. Data support the straight line $\Omega_0 = \Omega_M + \Omega_\Lambda = 1$, where Ω_M is the matter density in the Universe and Ω_Λ is the contribution of the nonzero cosmological constant (the energy density of the vacuum). At the same time one determines $\Omega_M = 0.4 \pm 0.1$, which implies $\Omega_\Lambda = 0.85 \pm 0.2$, a value that has been supported from high-redshifted supernova data. Since the baryonic matter density is small, $\Omega_B = 0.05 \pm 0.005$, the values for matter density Ω_M give a Cold Dark Matter (CDM) density $\Omega_{\text{CDM}} \simeq 0.35 \pm 0.1$ [3].

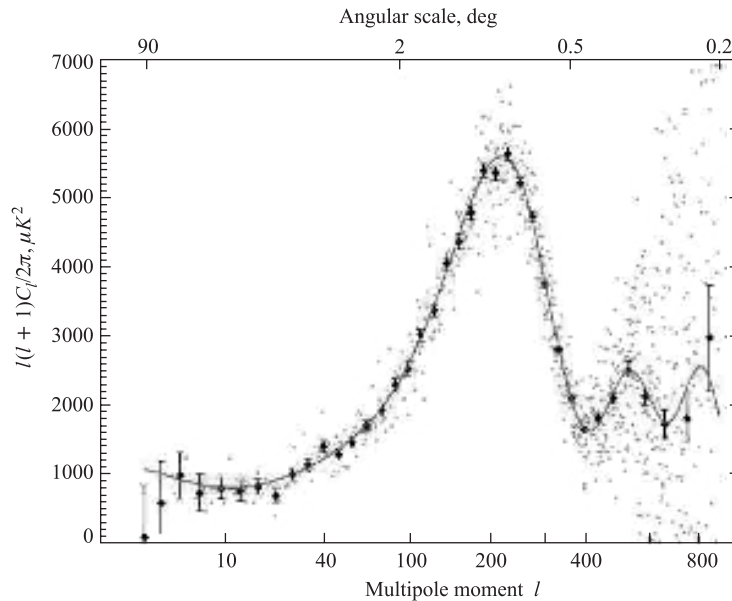


Fig. 3. The best fit power law Λ CDM model versus the WMAP temperature angular power spectrum [1, 2]

Recent Wilkinson Microwave Anisotropy Probe (WMAP) investigations [1, 2] of the cosmic microwave background and measurements of its temperature anisotropy (Fig. 3) supplied us with the most precise values for cosmological

parameters (Table 1). The parameters unambiguously confirm the existence of a big amount of the dark matter. Here we omit discussion of the dark energy — another mysterious substance in the Universe, which fills the gap between flat Universe and measured amount of dark matter ($\Omega_{\text{DM}} + \Omega_{\text{DE}} = \Omega_{\text{tot}} = 1$).

Table 1. Some basic and derived cosmological parameters

Hubble constant h	$0.71^{+0.04}_{-0.03}$
Baryon density $\Omega_b h^2$	0.0224 ± 0.0009
Matter density $\Omega_m h^2$	$0.135^{+0.008}_{-0.009}$
Neutrino density $\Omega_\nu h^2$	< 0.0076
Baryon/critical density Ω_b	0.044 ± 0.004
Matter/critical density Ω_m	0.27 ± 0.04
Total/critical density Ω_{tot}	1.02 ± 0.02
Age of the Universe t_0 , Gy	13.7 ± 0.2
Density of baryons n_b , cm^{-3}	$(2.5 \pm 0.1) \cdot 10^{-7}$
Baryon/photon ratio η	$(6.1^{+0.3}_{-0.2}) \cdot 10^{-10}$

According to the best estimate, the local density of this invisible matter amounts to about $\rho_{\text{local}}^{\text{DM}} \simeq 0.3 \text{ GeV}/\text{cm}^3 \simeq 5 \cdot 10^{-25} \text{ g}/\text{cm}^3$. It is assumed to have a Maxwellian velocity distribution with mean $\bar{v} \simeq 300 \text{ km/s}$. The local flux of DM particles χ is thus $\Phi_{\text{local}}^{\text{DM}} \simeq 100 \text{ GeV}/m_\chi \cdot 10^5 \text{ cm}^{-2} \cdot \text{s}^{-1}$. This not-small-enough value is considered as a basis for a direct search for dark matter particles.

Weakly Interacting Massive Particles (WIMPs) are among the most popular candidates for the relic cold dark matter. The main efforts and expectations in the direct dark matter searches are concentrated in the field of the so-called spin-independent (or scalar) interaction of a dark matter WIMP with a target nucleus. The lightest supersymmetric (SUSY) particle (LSP), neutralino, is assumed to be the best WIMP dark matter candidate. It is believed that for heavy enough nuclei this spin-independent (SI) interaction of DM particles with nuclei usually gives the dominant contribution to the expected event rate of its detection. The reason is the strong (proportional to the squared mass of the target nucleus) enhancement of SI WIMP–nucleus interaction. These results currently obtained in the field are usually presented in the form of exclusion curves due to nonobservation of the WIMPs (Fig. 4). For a fixed mass of the WIMP the cross sections of SI elastic WIMP–nucleon interaction located above these curves are excluded.

Only the DAMA (DARk MATter) collaboration claims observation of the first evidence for the dark matter signal, due to registration of the annual modulation effect [6–8]. The DAMA results are shown in the middle of Fig. 4 as two contours together with some set of other exclusion curves already obtained (solid lines) and expected in the future (dashed lines). Aimed since more than one decade at the

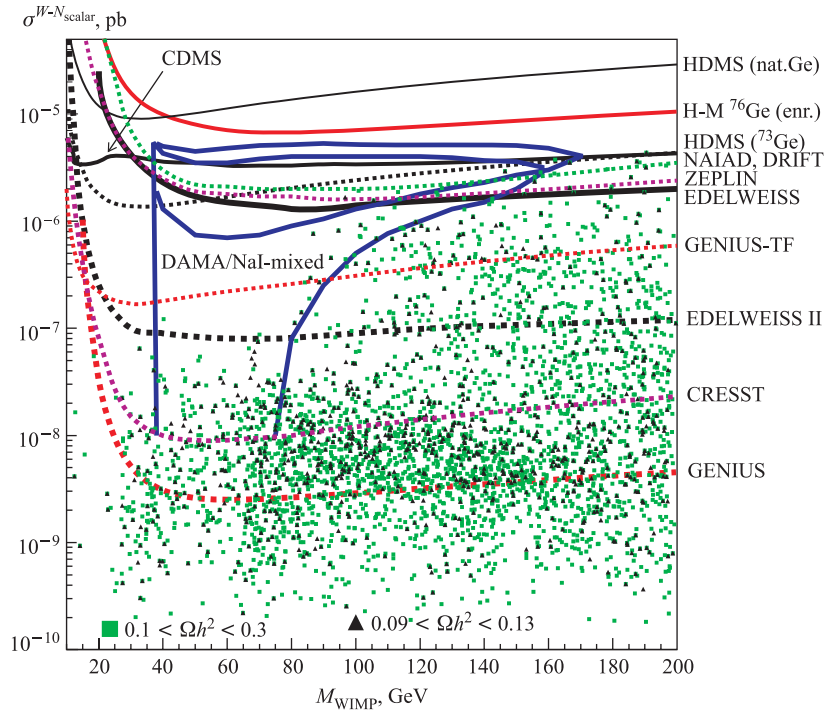


Fig. 4. WIMP–nucleon cross section limits in pb for scalar (spin-independent) interactions as a function of the WIMP mass in GeV. Shown are contour lines for some of the present experimental limits (solid lines) and some of projected experiments (dashed lines). The closed DAMA/NaI contour corresponds to a complete neglect of spin-dependent WIMP–nucleon interaction ($\sigma_{SD} = 0$), while the open contour is obtained with the assumption that $\sigma_{SD} = 0.08$ pb [7]. Our theoretical expectations are shown by scatter plots for a relic neutralino density $0.1 < \Omega_\chi h_0^2 < 0.3$ (grey squares) and to WMAP relic density $0.094 < \Omega_\chi h_0^2 < 0.129$ (black triangles). One can find similar estimations, for example, in [9–11]

DM-particle direct detection, the DAMA experiment (DAMA/NaI) with 100 kg of highly radiopure NaI(Tl) scintillator detectors successfully operated till July 2002 at the Gran Sasso National Laboratory of the INFN. On the basis of the results obtained over 7 annual cycles (107731 kg · day total exposure) the presence of a WIMP model-independent annual modulation signature was demonstrated, and the WIMP presence in the galactic halo is strongly supported at 6.3σ C.L. [7]. The main result of the DAMA observation of the annual modulation signature is the low-mass region of the WIMPs ($40 < m_\chi < 150$ GeV) and relatively high allowed SI or/and SD cross sections (for example, $1 \cdot 10^{-7} < \sigma_{SI}^p(0) < 3 \cdot 10^{-5}$ pb),

provided these WIMPs are cold dark matter particles. Although there are very good other experiments like EDELWEISS, CDMS, etc., which give sensitive exclusion curves, no one of them at present has the sensitivity to look for the modulation effect. Due to the small target masses and short running times the CDMS and EDELWEISS are unable to see positive annual modulation signature of the WIMP interactions. Often the results of these and DAMA experiments have been compared not on the basis of complete analysis including simultaneously SI and SD WIMP–nucleus interaction (see below). This sometimes gives rise to quite some confusion in literature. There are also other attempts to reconcile the DAMA conflict with the other experiments [12–16].

It is obvious that such a serious claim should be verified at least by one other completely independent experiment. To confirm this DAMA result one should perform a new experiment which would have (in reasonable time) the same or better sensitivity to the annual modulation signal (and also it would be better to locate this new setup in another low-background underground laboratory). This mission, in particular, could be executed by new-generation experiments with large enough mass of germanium high purity (HP) detectors both with spin (^{73}Ge) and spinless (natural Ge). Due to kinematic reasons ($M_{\text{targ}} \approx M_{\text{WIMP}}$) these germanium isotopes with their masses being almost equal to the mass of the DAMA WIMP (about 70 GeV) have the best efficiency for such WIMP detection. For example, a new setup with «naked» Ge detectors in liquid nitrogen (GENIUS-TF) is already installed and worked over months under the low-background conditions of the Gran Sasso Laboratory [17]. The GENIUS-TF experiment is planned to be sensitive to the annual modulation signal with data taking over about 5 years with a large enough mass of the Ge detectors [18]. Future EDELWEISS setup with 40-kg bolometric Ge detectors promises also to be sensitive to the annual modulation. In this paper, in particular, we start from the final results of the DAMA collaboration based on the 7-year-long measurements of the annual modulation [7] and consider their possible consequences for the dark matter search with high-spin ^{73}Ge detectors like HDMS [19] and some other heavy target detectors [20]. We also briefly consider some aspects of the spin-dependent (or axial-vector) interaction of the DM WIMPs with nuclei.

Historically, the spin-1/2 weakly interacting massive particles (WIMP) were considered as the first cold dark matter candidates. They interact with ordinary matter predominantly by means of axial vector (spin-dependent) and vector (spin-independent) couplings.

There is some revival of interest in the WIMP–nucleus spin-dependent interaction from both theoretical (see, e.g., [9, 21–27]) and experimental (see, e.g., [28–38]) points of view. There are some proposals aimed at direct DM detection with relatively low-mass isotope targets [28, 29, 34–37] as well as some attempts to design and construct a DM detector which is sensitive to the nuclear recoil direction [39–45]. Low-mass targets make preference for the low-mass

WIMPs and are more sensitive to the spin-dependent WIMP–nucleus interaction as well [9, 21, 23, 26, 46–48]. On the other hand, WIMPs with masses about $100 \text{ GeV}/c^2$ follow also from the results of the DAMA experiment.

In 1994, we claimed that nuclear spin is not important for detection of dark matter particles, provided the detection sensitivity does not exceed $0.01 \text{ events}/(\text{kg} \cdot \text{day})$, which was considered that time as unreachable [49]. Now the situation has changed and we would like to notice that for targets with spin-nonzero nuclei it might be the spin-dependent interaction that determines the lower bound for the direct detection rate when the cross section of the scalar interaction, which is usually assumed to be the dominant part, drops below $10^{-12 \div 13} \text{ pb}$ [50].

There are at least three reasons to think that SD (or axial-vector) interaction of the DM WIMPs with nuclei could be very important. First, contrary to the only one constraint for SUSY models available from the scalar WIMP–nucleus interaction, the spin WIMP–nucleus interaction supplies us with two such constraints (see, for example, [23] and formulas below). Second, one can notice [9, 24] that even with a very sensitive DM detector (say, with a sensitivity of $10^{-5} \text{ events}/(\text{kg} \cdot \text{day})$) which is sensitive only to the WIMP–nucleus scalar interaction (with spinless target nuclei) one can, in principle, miss a DM signal. To safely avoid such a situation one should have a spin-sensitive DM detector, i.e., a detector with spin-nonzero target nuclei. Finally, there is a complicated nuclear spin structure, which, for example, possesses the so-called long q -tail form-factor behavior. Therefore for heavy mass target nuclei and heavy WIMP masses the SD efficiency to detect a DM signal is much higher than the SI efficiency [21]. However, simultaneous study of both spin-dependent and spin-independent interactions of the DM particles with nuclei significantly increases the chance to observe the DM signal.

In Sec. 1 all formulas for event rate calculations are collected. In Sec. 2 the relevant to dark matter search spin nuclear structures are collected and discussed briefly. In Sec. 3 the effective low-energy minimal supersymmetric standard model (effMSSM) is used for calculation of the cross sections. It is also shown here that the low bound for the rate of direct dark matter detection is due to the spin-dependent WIMP–nucleon interaction and therefore one has to construct new-generation detectors with the nonzero spin target to avoid missing of the dark matter signal. In Sec. 4 the two experimental constraints from dark matter search with nonzero spin targets are discussed and two sets of exclusion curves for WIMP–proton and WIMP–neutron spin couplings are presented. In Sec. 5 the mixed spin–scalar couplings approach is argued, the DAMA-inspired exclusion domains for both the above-mentioned couplings are given and compared with SUSY calculations. The prospects for high-spin Ge-73 DM experiment are discussed in the mixed spin–scalar coupling scheme. In Sec. 6 some other consequences of the DAMA experiment are considered. Conclusion summarizes main results of the paper. Useful formulas are collected in Appendix.

1. EVENT RATE AND CROSS SECTIONS

One believes to detect directly a relic DM WIMP (or neutralino) χ with mass m_χ via its elastic scattering on a target nucleus (A, Z) . The nuclear recoil energy E_R is measured by a proper detector deeply underground (Fig. 5). The differential event rate in respect to the recoil energy is the subject of experimental measurements. The rate depends on the velocity distribution of the relic WIMPs in the solar vicinity $f(v)$ and the cross section of WIMP–nucleus elastic scattering [46, 48, 49, 51–55]. The differential event rate per unit mass of the target material has the form

$$\frac{dR}{dE_R} = N_T \frac{\rho_\chi}{m_\chi} \int_{v_{\min}}^{v_{\max}} dv f(v) v \frac{d\sigma^A}{dq^2}(v, q^2). \quad (1)$$

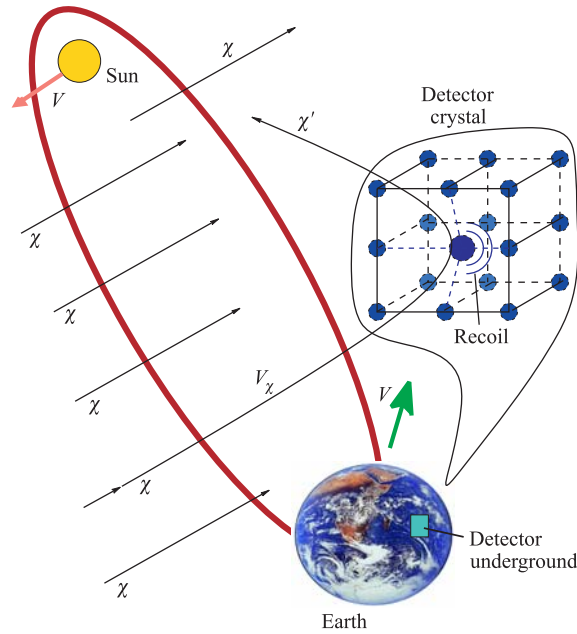


Fig. 5. Due to the expected annual modulation signature of the event rate (1) only the Sun–Earth system is a proper setup for the successful direct DM detection

We assume WIMPs (neutralinos) to be a dominant component of the DM halo of our Galaxy with a density $\rho_\chi = 0.3 \text{ GeV/cm}^3$ in the solar vicinity. The nuclear recoil energy $E_R = q^2/(2M_A)$ is typically about $10^{-6}m_\chi$, and N_T is the number density of a target nuclei with mass M_A , $v_{\max} = v_{\text{esc}} \approx 600 \text{ km/s}$, $v_{\min} = (M_A E_R / 2\mu_A^2)^{1/2}$.

The WIMP–nucleus differential elastic scattering cross section for spin-nonzero ($J \neq 0$) nuclei contains coherent (spin-independent, or SI) and axial (spin-dependent, or SD) terms [21, 56, 57]:

$$\frac{d\sigma^A}{dq^2}(v, q^2) = \frac{\sum |\mathcal{M}|^2}{\pi v^2(2J+1)} = \frac{d\sigma_{\text{SD}}^A}{dq^2}(v, q^2) + \frac{d\sigma_{\text{SI}}^A}{dq^2}(v, q^2) = \quad (2)$$

$$= \frac{S_{\text{SD}}^A(q^2)}{v^2(2J+1)} + \frac{S_{\text{SI}}^A(q^2)}{v^2(2J+1)} = \frac{S_{\text{SD}}^A(q^2)}{v^2(2J+1)} + \frac{\sigma_{\text{SI}}^A(0)}{4\mu_A^2 v^2} F_{\text{SI}}^2(q^2) = \quad (3)$$

$$= \frac{\sigma_{\text{SD}}^A(0)}{4\mu_A^2 v^2} F_{\text{SD}}^2(q^2) + \frac{\sigma_{\text{SI}}^A(0)}{4\mu_A^2 v^2} F_{\text{SI}}^2(q^2). \quad (4)$$

The normalized-to-unity ($F_{\text{SD,SI}}^2(0) = 1$) finite-momentum-transfer nuclear form factors

$$F_{\text{SD,SI}}^2(q^2) = \frac{S_{\text{SD,SI}}^A(q^2)}{S_{\text{SD,SI}}^A(0)} \quad (5)$$

can be expressed through the nuclear structure functions as follows [21, 56, 57]:

$$S_{\text{SI}}^A(q) = \sum_{L \text{ even}} |\langle J || \mathcal{C}_L(q) || J \rangle|^2 \simeq |\langle J || \mathcal{C}_0(q) || J \rangle|^2, \quad (6)$$

$$S_{\text{SD}}^A(q) = \sum_{L \text{ odd}} (|\langle N || \mathcal{T}_L^{\text{el}5}(q) || N \rangle|^2 + |\langle N || \mathcal{L}_L^5(q) || N \rangle|^2).$$

Here, the double vertical lines denote the reduced matrix element. The explicit form of the transverse electric $\mathcal{T}^{\text{el}5}(q)$ and longitudinal $\mathcal{L}^5(q)$ multipole projections of the axial vector current operator, scalar function $\mathcal{C}_L(q)$, and $S_{\text{SI,SD}}^A(q)$ at zero-momentum transfer can be found in Appendix. The spin-dependent structure functions are discussed in Sec. 2.

For the zero-momentum transfer, $q = 0$, the nuclear SD and SI cross sections (in (4)) can be presented as follows:

$$\sigma_{\text{SI}}^A(0) = \frac{4\mu_A^2 S_{\text{SI}}(0)}{(2J+1)} = \frac{\mu_A^2}{\mu_p^2} A^2 \sigma_{\text{SI}}^p(0), \quad (7)$$

$$\sigma_{\text{SD}}^A(0) = \frac{4\mu_A^2 S_{\text{SD}}(0)}{(2J+1)} = \frac{4\mu_A^2 (J+1)}{\pi J} \{a_p \langle \mathbf{S}_p^A \rangle + a_n \langle \mathbf{S}_n^A \rangle\}^2, \quad (8)$$

$$= \frac{\mu_A^2 (J+1)}{\mu_p^2 3J} \left\{ \sqrt{\sigma_{\text{SD}}^p(0)} \langle \mathbf{S}_p^A \rangle + \text{sign}(a_p a_n) \sqrt{\sigma_{\text{SD}}^n(0)} \langle \mathbf{S}_n^A \rangle \right\}^2, \quad (9)$$

$$= \frac{\mu_A^2 4J+1}{\mu_p^2 3J} \sigma_{\text{SD}}^{pn}(0) \{ \langle \mathbf{S}_p^A \rangle \cos \theta + \langle \mathbf{S}_n^A \rangle \sin \theta \}^2. \quad (10)$$

Following Bernabei et al. [7, 58] the effective spin WIMP–nucleon cross section $\sigma_{\text{SD}}^{pn}(0)$ and the coupling mixing angle θ were introduced

$$\sigma_{\text{SD}}^{pn}(0) = \frac{\mu_p^2}{\pi} \frac{4}{3} [a_p^2 + a_n^2], \quad \tan \theta = \frac{a_n}{a_p}; \quad (11)$$

$$\sigma_{\text{SD}}^p = \sigma_{\text{SD}}^{pn} \cos^2 \theta, \quad \sigma_{\text{SD}}^n = \sigma_{\text{SD}}^{pn} \sin^2 \theta. \quad (12)$$

Here, $\mu_A = \frac{m_\chi M_A}{m_\chi + M_A}$ is the reduced mass of the neutralino and the nucleus and it is assumed that $\mu_n^2 = \mu_p^2$. The dependence on effective WIMP–quark (in SUSY neutralino–quark) couplings \mathcal{C}_q and \mathcal{A}_q in the underlying theory (see Appendix)

$$\mathcal{L}_{\text{eff}} = \sum_q (\mathcal{A}_q \bar{\chi} \gamma_\mu \gamma_5 \chi \bar{q} \gamma^\mu \gamma_5 q + \mathcal{C}_q \bar{\chi} \chi \bar{q} q) + \dots \quad (13)$$

and on the spin ($\Delta_q^{(p,n)}$) and the mass ($f_q^{(p)} \approx f_q^{(n)}$) structure of the proton and neutron enter into these formulas via the zero-momentum-transfer WIMP–proton and WIMP–neutron SI and SD cross sections:

$$\sigma_{\text{SI}}^p(0) = 4 \frac{\mu_p^2}{\pi} c_0^2, \quad c_0 = c_0^{p,n} = \sum_q \mathcal{C}_q f_q^{(p,n)}; \quad (14)$$

$$\sigma_{\text{SD}}^{p,n}(0) = 12 \frac{\mu_{p,n}^2}{\pi} a_{p,n}^2, \quad a_p = \sum_q \mathcal{A}_q \Delta_q^{(p)}, \quad a_n = \sum_q \mathcal{A}_q \Delta_q^{(n)}. \quad (15)$$

The factors $\Delta_q^{(p,n)}$, which parameterize the quark-spin content of the nucleon, are defined as $2\Delta_q^{(n,p)} s^\mu \equiv \langle p, s | \bar{\psi}_q \gamma^\mu \gamma_5 \psi_q | p, s \rangle_{(p,n)}$.

The $\langle \mathbf{S}_{p(n)}^A \rangle$ is the total spin of protons (neutrons) averaged over all A nucleons of the nucleus (A, Z):

$$\langle \mathbf{S}_{p(n)}^A \rangle \equiv \langle A | \mathbf{S}_{p(n)}^A | A \rangle = \left\langle A \left| \sum_i^A \mathbf{s}_{p(n)}^i \right| A \right\rangle. \quad (16)$$

The expectation values of the spin and angular operators are evaluated, as a rule, in their z projection by assuming the state with the maximal value of the angular momentum projection $M_J = J$:

$$\langle \mathbf{S} \rangle \equiv \langle A | \mathbf{S} | A \rangle \equiv \langle J, M_J = J | S_z | J, M_J = J \rangle. \quad (17)$$

The mean velocity $\langle v \rangle$ of the relic neutralinos of our Galaxy is about $300 \text{ km/s} = 10^{-3}c$. Assuming $q_{\text{max}} R \ll 1$, where R is the nuclear radius and $q_{\text{max}} = 2\mu_A v$

is the maximum of the momentum transfer in the process of the χA scattering, the spin-dependent matrix element takes a simple form (*zero-momentum transfer limit*) [59,60]:

$$\mathcal{M} = C \langle A | a_p \mathbf{S}_p + a_n \mathbf{S}_n | A \rangle \mathbf{s}_\chi = C \Lambda \langle A | \mathbf{J} | A \rangle \mathbf{s}_\chi. \quad (18)$$

Here, \mathbf{s}_χ denotes the spin of the neutralino, and

$$\begin{aligned} \Lambda &= \frac{\langle N | a_p \mathbf{S}_p + a_n \mathbf{S}_n | N \rangle}{\langle N | \mathbf{J} | N \rangle} = \frac{\langle N | (a_p \mathbf{S}_p + a_n \mathbf{S}_n) \mathbf{J} | N \rangle}{J(J+1)} = \\ &= \frac{a_p \langle \mathbf{S}_p \rangle}{J} + \frac{a_n \langle \mathbf{S}_n \rangle}{J}. \end{aligned} \quad (19)$$

Note a coupling of the spin of χ to the spin carried by the protons and the neutrons. The uncertainties arising from the electroweak and QCD scale physics are incorporated in the factors a_p and a_n . The normalization factor C involves the coupling constants, the masses of the exchanged bosons and the mixing parameters relevant to the lightest supersymmetric particle (LSP), i.e., it is not related to the associated nuclear matrix elements [61]. The above conclusions concerning the spin-dependent part of the neutralino–nucleus scattering amplitude are also valid for the amplitude of any Majorana WIMP–nucleus scattering process. In the limit of zero-momentum transfer $q = 0$ the spin structure function in Eq. (6) reduces to the form

$$S^A(0) = \frac{1}{4\pi} \left| \langle A | \sum_i \frac{1}{2} (a_0 + a_1 \tau_3^i) \sigma_i | A \rangle \right|^2 = \frac{2J+1}{\pi} J(J+1) \Lambda^2.$$

The nuclear matrix element \mathcal{M} in Eq. (18) is often related to the matrix element of the nuclear magnetic moment, which also consists of the matrix elements of the total proton and neutron spin operators:

$$\mu = \langle A | g_n^s \mathbf{S}_n + g_n^l \mathbf{L}_n + g_p^s \mathbf{S}_p + g_p^l \mathbf{L}_p | A \rangle. \quad (20)$$

The *free particle* g factors (gyromagnetic ratios) are (in nuclear magnetons): $g_n^s = -3.826$, $g_n^l = 0$, $g_p^s = 5.586$, $g_p^l = 1$. The nuclear magnetic moment μ is often used as a benchmark for the accuracy of the calculation of \mathbf{S}_p and \mathbf{S}_n [57,60]. For the most interesting isotopes either $\langle \mathbf{S}_p^A \rangle$ or $\langle \mathbf{S}_n^A \rangle$ dominates ($\langle \mathbf{S}_{n(p)}^A \rangle \ll \langle \mathbf{S}_{p(n)}^A \rangle$). See, for example, Table 2.

As m_χ increases, $R \approx 1/q$ (the product qR starts to become non-negligible) and the *finite-momentum transfer limit* must be considered. The formalism is a straight forward extension of that developed for the study of weak and electromagnetic semileptonic interactions in nuclei [57,60]. With the isoscalar spin coupling constant $a_0 = a_n + a_p$ and the isovector spin coupling constant $a_1 = a_p - a_n$ one

Table 2. Zero-momentum spin structure of nuclei in different models. The measured magnetic moments used as input are enclosed in parentheses [26]

Model, authors and references	$\langle S_p \rangle$	$\langle S_n \rangle$	μ (in μ_N)
^{19}F ($L_J = S_{1/2}$)			
ISPSM, Ellis–Flores [62, 63]	1/2	0	2.793
OGM, Engel–Vogel [64]	0.46	0	(2.629) _{exp}
EOGM ($g_A/g_V = 1$), Engel–Vogel [64]	0.415	-0.047	(2.629) _{exp}
EOGM ($g_A/g_V = 1.25$), Engel–Vogel [64]	0.368	-0.001	(2.629) _{exp}
SM, Pacheco–Strottman [65]	0.441	-0.109	
SM, Divari et al. [47]	0.4751	-0.0087	2.91
^{23}Na ($L_J = P_{3/2}$)			
ISPSM	1/2	0	3.793
SM, Ressel–Dean [60]	0.2477	0.0198	2.2196
OGM, Ressel–Dean [60]	0.1566	0.0	(2.218) _{exp}
SM, Divari et al. [47]	0.2477	0.0199	2.22
^{27}Al ($L_J = D_{5/2}$)			
ISPSM, Ellis–Flores [62, 63]	1/2	0	4.793
OGM, Engel–Vogel [64]	0.25	0	(3.642) _{exp}
EOGM ($g_A/g_V = 1$), Engel–Vogel [64]	0.333	0.043	(3.642) _{exp}
EOGM ($g_A/g_V = 1.25$), Engel–Vogel [64]	0.304	0.072	(3.642) _{exp}
SM, Engel et al. [59]	0.3430	0.0296	3.584
^{73}Ge ($L_J = G_{9/2}$)			
ISPSM, Ellis–Flores [62, 63]	0	0.5	-1.913
OGM, Engel–Vogel [64]	0	0.23	(-0.879) _{exp}
IBFM, Iachello et al. [66] and [57]	-0.009	0.469	-1.785
IBFM (quenched), Iachello et al. [66] and [57]	-0.005	0.245	(-0.879) _{exp}
TFFS, Nikolaev–Klapdor–Kleingrothaus, [67]	0	0.34	—
SM (small), Ressel et al. [57]	0.005	0.496	-1.468
SM (large), Ressel et al. [57]	0.011	0.468	-1.239
SM (large, quenched), Ressel et al. [57]	0.009	0.372	(-0.879) _{exp}
«Hybrid» SM, Dimitrov et al. [68]	0.030	0.378	-0.920
^{127}I ($L_J = D_{5/2}$)			
ISPSM, Ellis–Flores [63, 69]	1/2	0	4.793
OGM, Engel–Vogel [64]	0.07	0	(2.813) _{exp}
IBFM, Iachello et al. [66]	0.464	0.010	(2.813) _{exp}
IBFM (quenched), Iachello et al. [66]	0.154	0.003	(2.813) _{exp}
TFFS, Nikolaev–Klapdor–Kleingrothaus, [67]	0.15	0	—
SM (Bonn A), Ressel–Dean [60]	0.309	0.075	2.775 {2.470} _{eff}
SM (Nijmegen II), Ressel–Dean [60]	0.354	0.064	3.150 {2.7930} _{eff}
^{131}Xe ($L_J = D_{3/2}$)			
ISPSM, Ellis–Flores [62, 63]	0	-0.3	1.148
OGM, Engel–Vogel [64]	0.0	-0.18	(0.692) _{exp}
IBFM, Iachello et al. [66]	0.000	-0.280	(0.692) _{exp}
IBFM (quenched), Iachello et al. [66]	0.000	-0.168	(0.692) _{exp}
TFFS, Nikolaev–Klapdor–Kleingrothaus, [67]		-0.186	—
SM (Bonn A), Ressel–Dean [60]	-0.009	-0.227	0.980 {0.637} _{eff}
SM (Nijmegen II), Ressel–Dean [60]	-0.012	-0.217	0.979 {0.347} _{eff}
QTDA, Engel [21]	-0.041	-0.236	0.70

can split the nuclear structure function $S^A(q)$ into a pure isoscalar term, $S_{00}^A(q)$, a pure isovector term, $S_{11}^A(q)$, and an interference term, $S_{01}^A(q)$, in the following way:

$$S^A(q) = a_0^2 S_{00}^A(q) + a_1^2 S_{11}^A(q) + a_0 a_1 S_{01}^A(q). \quad (21)$$

These three partial structure functions contain expectation values of operators of the form $j_L(qr)[Y_L \sigma]^{L\pm 1}$, which depend on spatial coordinates and nucleon spins. The relations

$$S_{00}^A(0) = C(J)(\langle \mathbf{S}_p \rangle + \langle \mathbf{S}_n \rangle)^2, \quad S_{11}^A(0) = C(J)(\langle \mathbf{S}_p \rangle - \langle \mathbf{S}_n \rangle)^2, \quad (22)$$

$$S_{01}^A(0) = 2C(J)(\langle \mathbf{S}_p^2 \rangle - \langle \mathbf{S}_n^2 \rangle) \quad \text{with} \quad C(J) = \frac{2J+1}{4\pi} \frac{J+1}{J}$$

connect the nuclear spin structure function $S^A(q)$ at $q = 0$ with proton $\langle \mathbf{S}_p \rangle$ and neutron $\langle \mathbf{S}_n \rangle$ spin contributions averaged over the nucleus. In relations (22) the normalization coefficient $C(J) > 0$ and therefore $S_{00}(0) \geq 0$ and $S_{11}(0) \geq 0$. These three partial structure functions $S_{ij}^A(q)$ (see the next Section) allow calculation of spin-dependent cross sections for any heavy Majorana particle as well as for the neutralino with arbitrary composition [59].

The differential event rate per unit mass of the target material (1) can be given also in the form [7, 70]:

$$\frac{dR(E_R)}{dE_R} = \kappa_{\text{SI}}(E_R, m_\chi) \sigma_{\text{SI}} + \kappa_{\text{SD}}(E_R, m_\chi) \sigma_{\text{SD}}. \quad (23)$$

$$\kappa_{\text{SI}}(E_R, m_\chi) = N_T \frac{\rho_\chi M_A}{2m_\chi \mu_p^2} B_{\text{SI}}(E_R) [M_A^2],$$

$$\begin{aligned} \kappa_{\text{SD}}(E_R, m_\chi) &= \\ &= N_T \frac{\rho_\chi M_A}{2m_\chi \mu_p^2} B_{\text{SD}}(E_R) \left[\frac{4}{3} \frac{J+1}{J} (\langle \mathbf{S}_p \rangle \cos \theta + \langle \mathbf{S}_n \rangle \sin \theta)^2 \right], \quad (24) \end{aligned}$$

$$B_{\text{SI,SD}}(E_R) = \frac{\langle v \rangle}{\langle v^2 \rangle} F_{\text{SI,SD}}^2(E_R) I(E_R).$$

The dimensionless integral $I(E_R)$ is dark-matter-particle velocity distribution correction:

$$\begin{aligned} I(E_R) &= \frac{\langle v^2 \rangle}{\langle v \rangle} \int_{x_{\min}} \frac{f(x)}{v} dx = \\ &= \frac{\sqrt{\pi}}{2} \frac{3 + 2\eta^2}{\sqrt{\pi}(1 + 2\eta^2)\text{erf}(\eta) + 2\eta e^{-\eta^2}} [\text{erf}(x_{\min} + \eta) - \text{erf}(x_{\min} - \eta)], \end{aligned}$$

where we assume that in our Galaxy rest frame WIMPs have the Maxwell–Boltzmann velocity distribution and use the dimensionless Earth speed with respect to the halo $\eta = 1$, $x_{\min}^2 = \frac{3}{4} \frac{M_A E_R}{\mu_A^2 \bar{v}^2}$. The error function is $\text{erf}(x) =$

$\frac{2}{\sqrt{\pi}} \int_0^x dt e^{-t^2}$. The velocity variable is the dispersion $\bar{v} \simeq 270$ km/s. The mean

WIMP velocity $\langle v \rangle = \sqrt{\frac{5}{3}} \bar{v}$. We also assume both form factors $F_{\text{SI,SD}}^2(E_R)$ in the simplest Gaussian form following [62, 63]. In particular, this allows rather simple formulas (24) to be used, which are suitable for our comparative consideration. Integrating the differential rate (1) from the recoil energy threshold ϵ to some maximal energy ε one obtains the total detection rate $R(\epsilon, \varepsilon)$ as a sum of the SD and SI terms:

$$R(\epsilon, \varepsilon) = R_{\text{SI}}(\epsilon, \varepsilon) + R_{\text{SD}}(\epsilon, \varepsilon) = \int_{\epsilon}^{\varepsilon} dE_R \kappa_{\text{SI}}(E_R, m_\chi) \sigma_{\text{SI}} + \int_{\epsilon}^{\varepsilon} dE_R \kappa_{\text{SD}}(E_R, m_\chi) \sigma_{\text{SD}} = \alpha(\epsilon, \varepsilon, m_\chi) \sigma_{\text{SI}}^p + \beta(\epsilon, \varepsilon, m_\chi) \sigma_{\text{SD}}^{pn}; \quad (25)$$

$$\alpha(\epsilon, \varepsilon, m_\chi) = N_T \frac{\rho_\chi M_A}{2m_\chi \mu_p^2} A^2 A_{\text{SI}}(\epsilon, \varepsilon),$$

$$\beta(\epsilon, \varepsilon, m_\chi) = N_T \frac{\rho_\chi M_A}{2m_\chi \mu_p^2} \frac{4}{3} \frac{J+1}{J} (\langle \mathbf{S}_p^A \rangle \cos \theta + \langle \mathbf{S}_n^A \rangle \sin \theta)^2 A_{\text{SD}}(\epsilon, \varepsilon);$$

$$A_{\text{SI,SD}}(\epsilon, \varepsilon) = \frac{\langle v \rangle}{\langle v^2 \rangle} \int_{\epsilon}^{\varepsilon} dE_R F_{\text{SI,SD}}^2(E_R) I(E_R). \quad (26)$$

To accurately estimate the event rate $R(\epsilon, \varepsilon)$ one needs to know a number of quite uncertain astrophysical and nuclear structure parameters as well as the very specific characteristics of an experimental setup (see, for example, discussions in [7, 71]).

2. NUCLEAR SPIN STRUCTURE AT FINITE-MOMENTUM TRANSFER

The modern nuclear spin structure calculations involved into the problem of the direct dark matter search are reviewed in [26, 72]. Both these reviews together can be considered as some guide over currently available nuclear spin structure

results involved in the problem. The calculations of the proton and neutron spins $\langle \mathbf{S}_{p(n)} \rangle$ averaged over all nucleons in the nucleus A , which are relevant to the zero-momentum neutralino–nucleon spin cross sections, are considered in [26]. The cross sections at zero-momentum transfer show strong dependence on the nuclear structure of the ground state [47]. The calculations of the spin structure functions in the *finite*-momentum transfer approximation are discussed in [72]. All available sets of the spin structure functions are collected in [72] either in the form of explicit functions or as useful analytical parameterizations of the accurate numerical results, or only graphically (as pictures from original papers). These functions describe recoil energy dependence of the differential event rate due to spin-dependent neutralino–nucleon interaction, provided neutralino is a dark-matter particle. To the best of our knowledge, the finite, nonzero-momentum transfer calculations of the spin nuclear structure functions $S^A(q)$ have been performed for the isotopes given in Table 3.

Table 3. List of isotopes with available spin structure functions, $S^A(q)$, at $q > 0$

A	Isotope	Authors and reference(s)
19	Fluorine, ^{19}F	Vergados et al. [45, 47, 73]
23	Sodium, ^{23}Na	Ressell and Dean [60] Vergados et al. [47, 60]
27	Aluminium, ^{27}Al	Engel et al. [59]
29	Silicon, ^{29}Si	Ressell et al. [57] Vergados et al. [45, 47]
39	Potassium, ^{39}K	Engel et al. [59]
73	Germanium, ^{73}Ge	Ressell et al. [57] Demitrov et al. [68]
93	Niobium, ^{93}Nb	Engel et al. [74]
123	Tellurium, ^{123}Te	Nikolaev and Klapdor-Kleingrothaus [75]
125	Tellurium, ^{125}Te	Ressell and Dean [60]
127	Iodine, ^{127}I	Ressell and Dean [60]
129	Xenon, ^{129}Xe	Ressell and Dean [60]
131	Xenon, ^{131}Xe	Engel [21] Ressell and Dean [60] Nikolaev and Klapdor-Kleingrothaus [75]
207	Lead, ^{207}Pb	Vergados and Kosmos [73, 76]

As already noted for quite heavy WIMPs and sufficiently heavy nuclei, the dependence of the nuclear matrix elements on the momentum transfer cannot be ignored even if the WIMP has energies as low as 100 keV. For example, if $m_\chi \gg m_A$, the reduced mass μ_A almost reaches m_A ($\mu_A \rightarrow m_A$). It is rather popular (and the simplest) assumption that the WIMPs have a Maxwellian velocity distribution in the halo of our Galaxy. Some WIMPs will possess velocities significantly greater than $\langle v \rangle \simeq 10^{-3}c$. A maximum velocity of $v_{\max} \simeq 700$ km/s (slightly greater than the Galactic escape velocity and more than twice the mean WIMP velocity) implies maximum momentum transfers of $q_{\max} \simeq 550$ MeV for nuclei with atomic weight $A \sim 127$. This q value is not *small* compared to the inverse nuclear size [60] and one has to use *the finite-momentum transfer approximation* for heavier nuclei.

The first model to estimate the spin content in the nucleus for the dark matter search was the independent single-particle shell model (ISPSM) used originally by Goodman and Witten [77] and later in [52,62,78]. Here the ground-state value of the nuclear total spin J can be described by that of one extra nucleon interacting with the effective potential of the nuclear core. There are nuclear structure calculations (including nonzero-momentum approximation) for spin-dependent neutralino interaction with helium ^3He [73]; fluorine ^{19}F [45,47,73]; sodium ^{23}Na [45,47,60,73]; aluminum ^{27}Al [59]; silicon ^{29}Si [45,47,57]; chlorine ^{35}Cl [57]; potassium ^{39}K [59]; germanium ^{73}Ge [57,68]; niobium ^{93}Nb [74]; iodine ^{127}I [60]; xenon ^{129}Xe [60] and ^{131}Xe [21,60,75]; tellurium ^{123}Te [75] and ^{125}Te [60]; lead ^{208}Pb [73,76]. The zero-momentum transfer limit (mostly quenching) is also investigated for Cd, Cs, Ba, and La [65,66,75], for hydrogen, ^1H [62,63], helium, ^3He [73], chlorine, ^{35}Cl [57], and calcium, ^{43}Ca [51].

There are several approaches to more accurate calculations of the nuclear structure effects relevant to the dark-matter detection. The list of the models includes the Odd Group Model (OGM) of Engel and Vogel [64] and their extended OGM (EOGM) [56,64]; Interacting Boson Fermion Model (IBFM) of Iachello, Krauss, and Maino [66]; Theory of Finite Fermi Systems (TFFS) of Nikolaev and Klapdor-Kleingrothaus [67]; Quasi Tamm–Dancoff Approximation (QTDA) of Engel [21]; different shell model treatments (SM) by Pacheco and Strottman [65]; by Engel, Pittel, Ormand, and Vogel [74] and Engel, Ressel, Towner, and Ormand, [59], by Ressel et al. [57] and Ressel and Dean [60]; by Kosmas, Vergados et al. [47,73,76]; the so-called «hybrid» model of Dimitrov, Engel, and Pittel [68] and perturbation theory based on calculations of Engel et al. [59].

The full momentum dependence of the form factors must be calculated from detailed nuclear models, and the results are especially important for heavier nuclei [46]. Unfortunately, the simple phenomenological analysis in the OGM (odd group model) and EOGM (extended OGM) of [64] cannot be extended to the finite-momentum transfer case, because the experimental data directly related to

the neutralino–nucleus elastic scattering is not available [21]. Quite a number of high multipoles can now contribute, some of them getting contributions from components of the wave function which do not contribute in the static limit (i.e., at $q = 0$). Thus, in general, sophisticated shell model calculations are needed to account both for the observed retardation of the static spin matrix element and its correct dependence on transfer momentum, q . For the experimentally interesting nuclear systems ^{29}Si and ^{73}Ge , very elaborate calculations have been performed by Ressel et al. [57]. In the case of ^{73}Ge a further improved calculation by Dimitrov, Engel, and Pittel was carried out [68] by suitably mixing variationally determined triaxial Slatter determinants. Indeed, for this complex nucleus many multipoles contribute and the needed calculations involve techniques which are extremely sophisticated [76]. Now the necessity for more detailed calculations *especially* for the spin-dependent component of the cross sections for heavy nuclei is well motivated.

To perform modern data analysis in the finite-momentum transfer approximation it looks reasonable to use formulas for differential event rate (1) schematically given below:

$$\begin{aligned} \frac{dR(\epsilon, \varepsilon)}{dE_R} &= \frac{\rho}{m_{\tilde{\chi}} m_A} \int v dv f(v) \frac{8G_F^2}{(2J+1)v^2} S_{\text{SD}}^A(q) = \\ &= \mathcal{N}(\epsilon, \varepsilon, E_R, m_{\chi}) [\eta_{\text{SI}}(E_R, m_{\chi}) \sigma_{\text{SI}}^p + \eta'_{\text{SD}}(E_R, m_{\chi}, \omega) a_0^2]; \quad (27) \\ \mathcal{N}(\epsilon, \varepsilon, E_R, m_{\chi}) &= \left[N_T \frac{c\rho_{\chi}}{2m_{\chi}} \frac{M_A}{\mu_p^2} \right] \frac{4\mu_A^2}{\langle q_{\text{max}}^2 \rangle} \left\langle \frac{v}{c} \right\rangle I(E_R) \theta(E_R - \epsilon) \theta(\varepsilon - E_R); \\ \eta_{\text{SI}}(E_R, m_{\chi}) &= \{ A^2 F_{\text{SI}}^2(E_R) \}; \\ \eta'_{\text{SD}}(E_R, m_{\chi}, \omega) &= \mu_p^2 \left\{ \frac{4}{2J+1} (S_{00}(q) + \omega^2 S_{11}(q) + \omega S_{01}(q)) \right\}; \\ I(E_R) &= \int_0^{\infty} \frac{\langle v^2 \rangle}{\langle v \rangle} \frac{dv}{v} f(v) \theta(4\mu_A^2 v^2 - 2M_A E_R). \end{aligned}$$

Here the isovector-to-isoscalar nucleon couplings ratio is $\omega = a_1/a_0$. In expressions (27) are introduced the detector threshold recoil energy ϵ and the maximal available recoil energy ε ($\epsilon \leq E_R \leq \varepsilon$). In practice, for example, with an ionization or scintillation signal, one has to take into account the quenching of the recoil energy, when visible recoil energy is smaller than the real recoil energy transmitted by the WIMP to the target nucleus. Formulas (27) allow experimental recoil spectra to be directly described in terms of only *three* [23] independent parameters (σ_{SI}^p , a_0^2 , and ω) for any fixed WIMP mass m_{χ} (and any neutralino

composition). Note, that today it is rather reasonable to assume $\sigma_{\text{SI}}^p(0) \approx \sigma_{\text{SI}}^n(0)$. Comparing this formula with the observed recoil spectra for different targets (Ge, Xe, F, NaI, etc.) one can directly and simultaneously restrict both isoscalar and isovector neutralino–nucleon effective couplings $a_{0,1}$. These constraints will impose the most model-independent restrictions on the MSSM parameter space. Contrary to some other possibilities (see, for example, this procedure is direct and uses as much as possible the results of the most accurate nuclear spin structure calculations.

Long-Tail q Behavior due to the Spin. An attractive feature of the SD WIMP–nucleus interaction is the q dependence of SD structure function (21). The ratio of SD to SI rate in the ^{73}Ge detector grows with the WIMP mass [9, 24]. The growth is much greater for heavy target isotopes like xenon. The reason is the different behavior of the spin and scalar structure functions with increasing momentum transfer. For example, the xenon SI structure function vanishes at recoil energy 80 keV, but the SD xenon structure functions (given in Fig. 6) are still nonzero in the region.

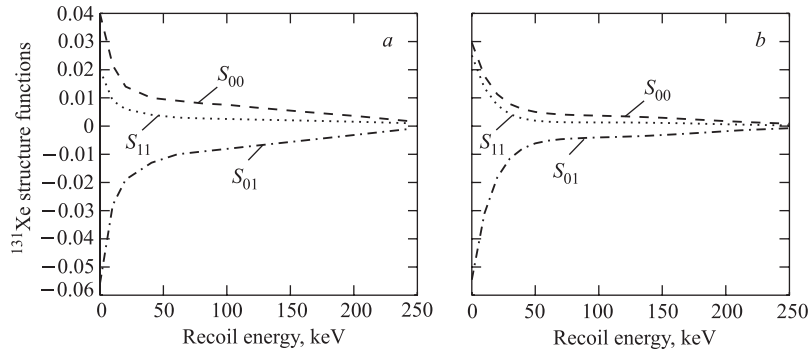


Fig. 6. Partial structure functions $S_{00}^{131}(q)$ (dashed line), $S_{01}^{131}(q)$ (dash-dotted line) and $S_{11}^{131}(q)$ (dotted line) in ^{131}Xe as a function of the recoil energy. *a*) Results of Engel [21]; *b*) the parameterizations of Ressel and Dean [60]. For ^{131}Xe , when the maximal WIMP velocity $v_{\text{max}} = 600$ km/s, one has $q_{\text{max}} \approx 487$ MeV/ c and $E_{\text{max}} \approx 963$ keV

For comparison, Fig. 7 shows the recoil energy dependence of the partial structure functions S_{00}^{73} , S_{11}^{73} , and S_{01}^{73} for ^{73}Ge calculated by Ressel et al. [57] (Fig. 7, *a*) and by Dimitrov, Engel, and Pittel [68] (Fig. 7, *b*). The structure functions completely determine the spin-dependent cross sections of elastic neutralino scattering off ^{73}Ge .

As noted by Engel in [21], the relatively long tail of the SD structure function is caused by nucleons near the Fermi surface, which do the bulk of the scattering.

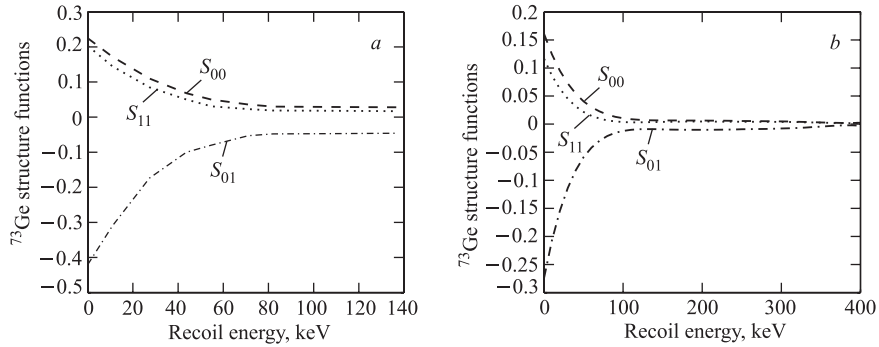


Fig. 7. Spin structure functions S_{00}^{73} (dashed line), S_{11}^{73} (dotted line), and S_{01}^{73} (dash-dotted line) for ^{73}Ge as a function of the recoil energy. *a*) Results of Russell et al. [57]; *b*) the same structure functions, but from the «hybrid» method of Dimitrov, Engel, and Pittel [68]. With $v_{\text{max}} \approx 600$ km/s, for the ^{73}Ge target one has $E_{\text{max}} \approx 537$ keV

The core nucleons, which dominate the SI nuclear coupling, contribute much less at large q . Therefore the SD efficiency for detection of a DM signal is higher than the SI efficiency, especially for very heavy neutralinos.

3. CROSS SECTIONS IN THE EFFECTIVE LOW-ENERGY MSSM

To estimate the expected direct DM detection rates (with formulas (1), (25) or (27)) one should calculate cross sections σ_{SI} and σ_{SD} (or more precisely WIMP–nucleon couplings $a_{p,n}$) within the framework of some SUSY-based theory or take them from experimental data.

To obtain as much as general SUSY predictions it appeared more convenient to work within a phenomenological SUSY model whose parameters are defined directly at the electroweak scale, relaxing completely constraints following from any unification assumption (see, for example, [3, 9, 24, 25, 48–50, 55, 80–85]). This effective scheme of the MSSM is called the effMSSM in [86], and later the low-energy effective supersymmetric theory (LEEST) in [10, 11]. In our previous calculations in effMSSM [9, 24, 25, 48–50, 55, 83–85] we have adopted some effective scheme (with nonuniversal scalar masses and with nonuniversal gaugino soft masses) which leads to rather large values for direct detection rates of DM neutralinos.

The effMSSM parameter space is determined by entries of the mass matrices of neutralinos, charginos, Higgs bosons, sleptons and squarks (see Appendix). The list of free parameters includes: $\tan \beta$ — the ratio of neutral Higgs boson

vacuum expectation values; μ — the bilinear Higgs parameter of the superpotential; $M_{1,2}$ — soft gaugino masses; M_A — the CP -odd Higgs mass; $m_{\tilde{Q}}^2$, $m_{\tilde{U}}^2$, $m_{\tilde{D}}^2$ ($m_{\tilde{L}}^2$, $m_{\tilde{E}}^2$) — squark (slepton) mass parameters squared for the 1st and 2nd generations; $m_{\tilde{Q}_3}^2$, $m_{\tilde{T}}^2$, $m_{\tilde{B}}^2$ ($m_{\tilde{L}_3}^2$, $m_{\tilde{\tau}}^2$) — squark (slepton) mass parameters squared for the 3rd generation; A_t , A_b , A_τ — soft trilinear couplings for the 3rd generation. The third gaugino mass parameter M_3 defines the mass of the gluino in the model and is determined by means of the GUT assumption $M_2 = 0.3M_3$. In the MSSM the lightest neutralino $\chi \equiv \tilde{\chi}_1^0$ is a mixture of four superpartners of gauge and Higgs bosons (Bino, Wino, and two Higgsinos):

$$\chi = N_{11}\tilde{B}^0 + N_{12}\tilde{W}^0 + N_{13}\tilde{H}_1^0 + N_{14}\tilde{H}_2^0. \quad (28)$$

It is commonly accepted that χ is mostly gaugino-like if $P \equiv N_{11}^2 + N_{12}^2 > 0.9$ and Higgsino-like if $P < 0.1$, or mixed otherwise.

We have included the current experimental upper limits on sparticle and Higgs masses from the Particle Data Group [87]. For example, we use as previously the following lower bounds for the SUSY particles: $M_{\tilde{\chi}_{1,2}^\pm} \geq 100$ GeV for charginos, $M_{\tilde{\chi}_{1,2,3}^0} \geq 45, 76, 127$ GeV for non-LSP neutralinos, respectively; $M_{\tilde{\nu}} \geq 43$ GeV for sneutrinos, $M_{\tilde{e}_R} \geq 70$ GeV for selectrons, $M_{\tilde{q}} \geq 210$ GeV for squarks, $M_{\tilde{t}_1} \geq 85$ GeV for light top-squark, $M_{H^0} \geq 100$ GeV for neutral Higgs bosons, $M_{H^\pm} \geq 70$ GeV for the charged Higgs boson. Also the limits on the rare $b \rightarrow s\gamma$ decay [88, 89] following [90–93] have been imposed.

For each point in the MSSM parameter space (MSSM model) the relic density of the light neutralinos $\Omega_\chi h^2$ was evaluated with the code [83–85] based on DarkSUSY [94] with the allowance for all coannihilation channels with two-body final states that can occur between neutralinos, charginos, sleptons, stops, and sbottoms as long as their masses are $m_i < 2m_\chi$.

Two cosmologically interesting regions were considered. One is $0.1 < \Omega_\chi h^2 < 0.3$ and the other is the WMAP-inspired region $0.094 < \Omega_\chi h^2 < 0.129$ [1, 2]. A possibility the LSP to be not a unique DM candidate with much smaller relic density $0.002 < \Omega h^2 < 0.1$ is also taken into account. Further details can be found in [70].

In numerical studies of [9, 83–85, 95], the parameters of the MSSM are randomly varied in the following intervals:

$$\begin{aligned} -1 < M_1 < 1 \text{ TeV}, \quad -2 < M_2, \mu, A_t < 2 \text{ TeV}, \\ 1 < \tan \beta < 50, \quad 60 < M_A < 1000 \text{ GeV}, \\ 10 < m_{\tilde{Q}}^2, m_{\tilde{L}}^2, m_{\tilde{Q}_3}^2, m_{\tilde{L}_3}^2 < 10^6 \text{ GeV}^2. \end{aligned} \quad (29)$$

Bounds on flavor-changing neutral currents imply that squarks with equal gauge quantum numbers must be close in mass [96–98]. With the possible exception

of the third generation squarks the assumed degeneracy holds almost model-independently [96]. Therefore for other sfermion mass parameters as before in [9, 24, 25, 50, 83–85] we used the relations $m_U^2 = m_D^2 = m_Q^2$, $m_E^2 = m_L^2$, $m_T^2 = m_B^2 = m_{Q_3}^2$, $m_{E_3}^2 = m_{L_3}^2$. The parameters A_b and A_τ are fixed to be zero. We consider the domain of the MSSM parameter space, in which we perform our scans, as quite spread and natural.

Our calculations for the WIMP–nucleon cross section of both spin and scalar interactions as a function of the WIMP mass for parameters (29) are depicted as scatter plots (Figs. 8–12). Scatter plots with individual cross sections of spin-dependent and spin-independent interactions of WIMPs with proton and neutron are given in Fig. 8 as functions of the LSP mass. In the figure light circles correspond to cross sections calculated under the old assumption that $0.025 < \Omega_\chi h_0^2 < 1$. Filled triangles give the same cross section but the constraint on the flat and accelerating Universe is imposed by $0.1 < \Omega_\chi h_0^2 < 0.3$. One can see that the reduction of the allowed domain for the relic density does not significantly affect spin-dependent and spin-independent WIMP–nucleon cross sections, i.e.,

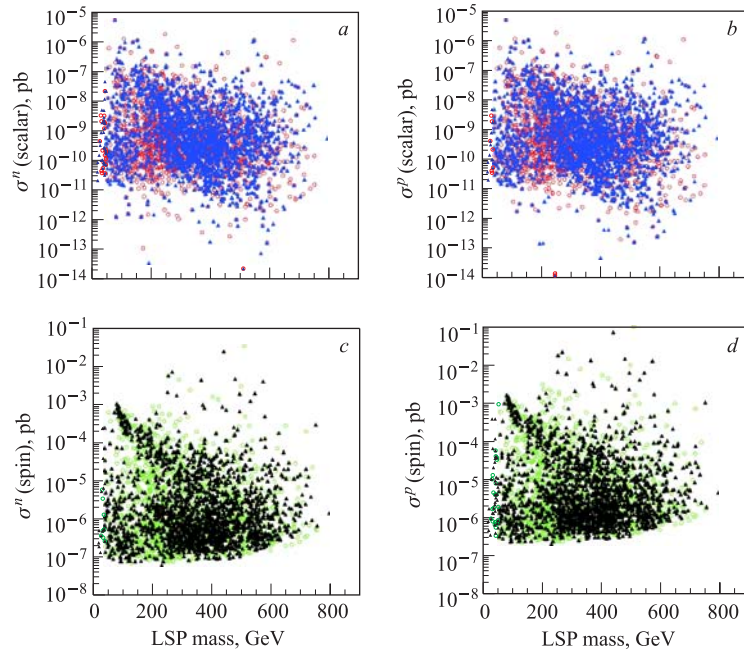


Fig. 8. Cross sections of spin-dependent and spin-independent interactions of WIMPs with proton (b, d) and neutron (a, c). Filled triangles (light circles) correspond to relic neutralino density $0.1 < \Omega_\chi h_0^2 < 0.3$ ($0.025 < \Omega_\chi h_0^2 < 1$)

restriction to a flat and accelerating Universe weakly affects these cross sections. The different behavior of these cross sections with mass of the LSP can be seen from the plots. There is a more stringent lower bound for the spin-dependent cross section. It is at a level of 10^{-7} pb.

As was noticed by many groups the scalar cross section of elastic WIMP–nucleon scattering increases with $\tan \beta$. The parameter $\tan \beta$ seems to be the only SUSY parameter with which the lower bound of the direct detection rate has the tendency to increase. The spin-dependent and spin-independent WIMP–proton cross sections as functions of input parameters μ , m_Q^2 , M_A , $\tan \beta$ are depicted in Figs. 9 and 10.

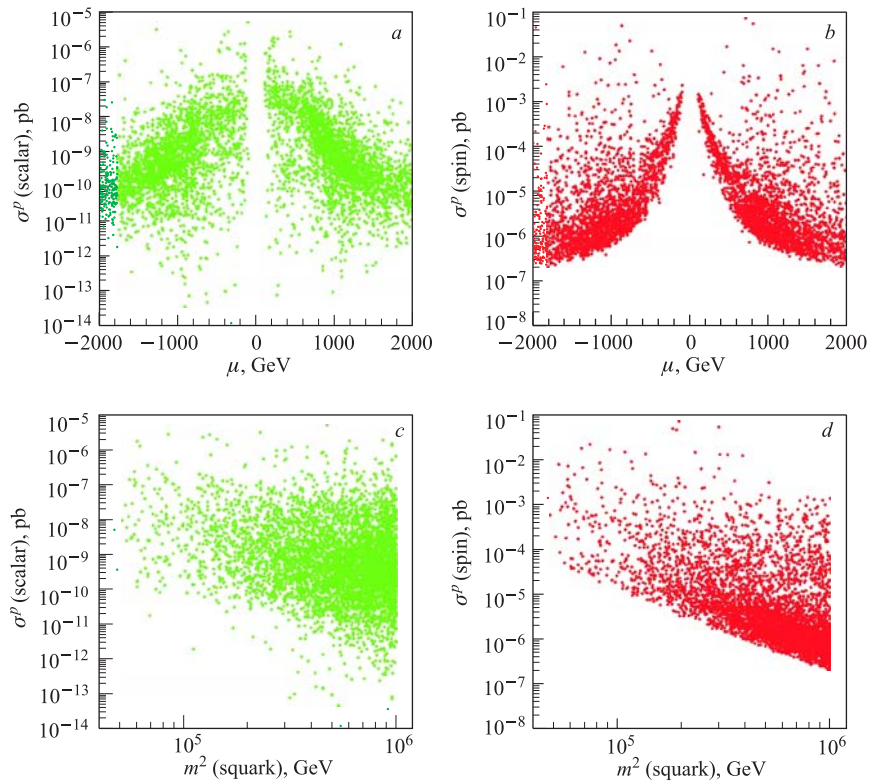


Fig. 9. Cross sections of WIMP–proton spin-dependent and spin-independent interactions as a function of input parameters μ (a, b) and m_Q^2 (c, d) obtained with $0.1 < \Omega_\chi h_0^2 < 0.3$

There is no noticeable dependence of these scatter plots on the other free parameters from (29), for which we therefore do not show scatter plots. One can see from Fig. 9 the similarity of the scatter plots for spin-dependent and scalar cross sections as functions of μ and m_Q^2 . The decrease of both lower bounds of

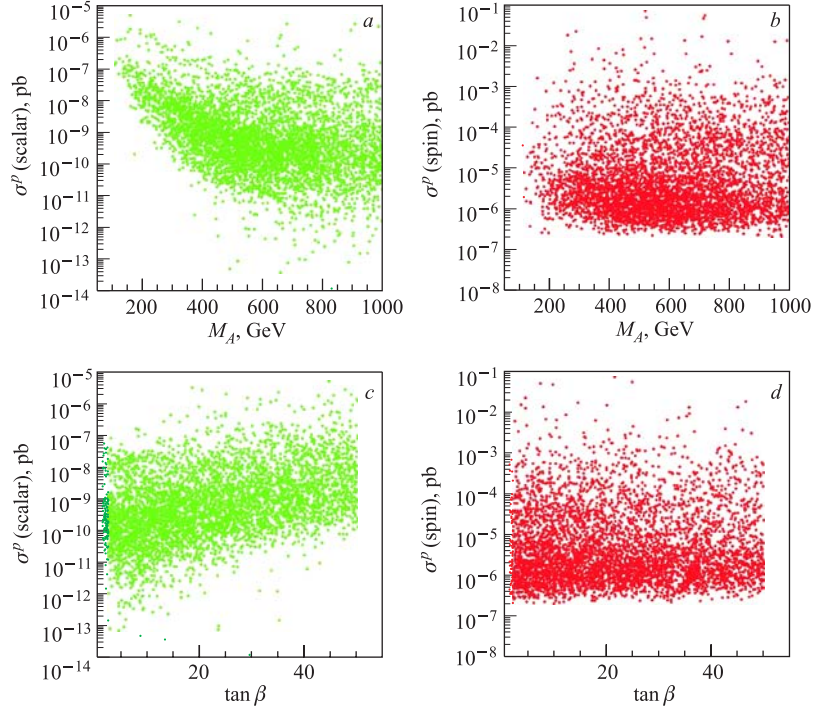


Fig. 10. Cross sections of WIMP–proton spin-dependent and spin-independent interactions as function of input parameters M_A (a, b) and $\tan \beta$ (c, d) obtained with $0.1 < \Omega_\chi h_0^2 < 0.3$

the cross sections with m_Q^2 occurs due to the increase of masses of squarks, which enter the s-channel intermediate states. The only visible difference concerns more sharp lower bounds for the spin-dependent cross section. Both spin-dependent and spin-independent cross sections increase when $|\mu|$ decreases.

The increase of the scalar cross sections generally is connected with the increase of the Higgsino admixture of the LSP and increase of Higgsino–gaugino interference which enters this cross section.

3.1. Cross Sections in the effMSSM for $m_\chi < 200$ GeV. For more accurate investigation of the DAMA-inspired domain of the lower masses of the LSP ($m_\chi < 200$ GeV) in [70], both σ_{SD} and σ_{SI} have also been calculated within the effMSSM. To this end the intervals of the randomly scanned MSSM parameter space in [70] were narrowed:

$$\begin{aligned} -200 < M_1 < 200 \text{ GeV}, \quad -1 < M_2, \mu < 1 \text{ TeV}, \quad -2 < A_t < 2 \text{ TeV}, \\ 10 < \tan \beta < 50, \quad 50 < M_A < 500 \text{ GeV}. \end{aligned} \quad (30)$$

The results of our evaluations of the zero-momentum-transfer proton and neutron SI (14) and SD (15) cross sections in the effMSSM approach within the DAMA-inspired parameter space of (30) are shown as scatter plots in Fig. 11. The figure is the WIMP low-mass updated analog of Fig. 8, which has been obtained in the full effMSSM parameter space (see (29)).

In Fig. 11 circles correspond to cross sections calculated when the neutralino relic density should just not overclose the Universe ($0.0 < \Omega_\chi h_0^2 < 1.0$). Squares show the same cross sections when one assumes the relic neutralinos to be not the only DM particles and give only subdominant contribution to the relic density $0.002 < \Omega_\chi h_0^2 < 0.1$. In Fig. 11, *a, c* these cross sections are shown with the

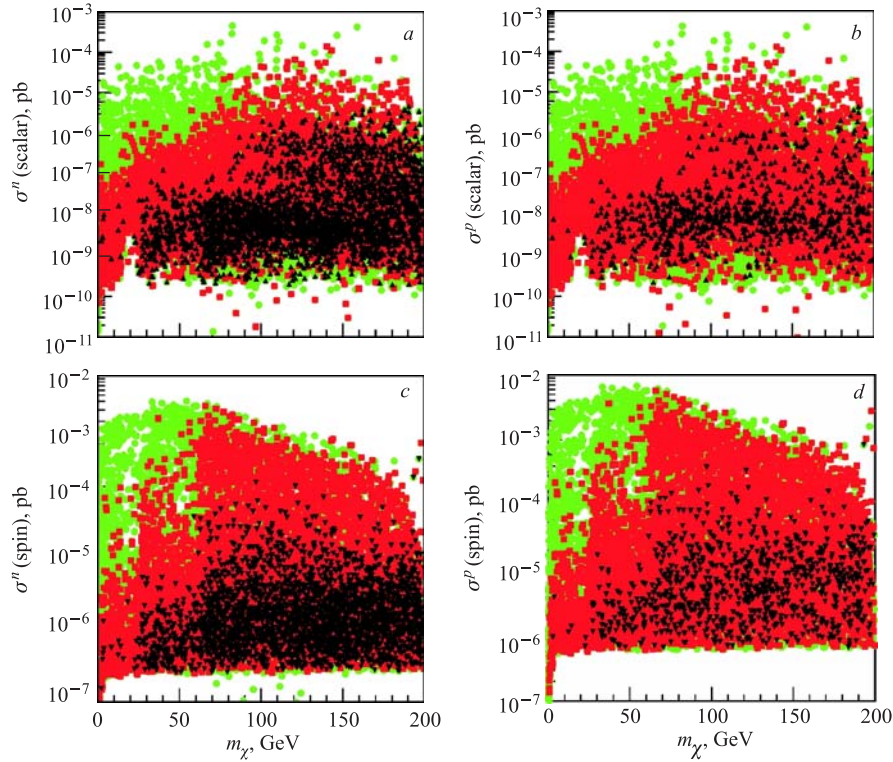


Fig. 11. Cross sections of the spin-dependent (spin) and the spin-independent (scalar) interactions of WIMPs with the proton and the neutron. Circles correspond to the relic neutralino density $0 < \Omega_\chi h_0^2 < 1$, squares correspond to the subdominant relic neutralino contribution $0.002 < \Omega_\chi h_0^2 < 0.1$ and black triangles correspond to the relic neutralino density $0.1 < \Omega_\chi h_0^2 < 0.3$ (*a, c*) and to the WMAP relic density $0.094 < \Omega_\chi h_0^2 < 0.129$ (*b, d*)

black triangles corresponding to the case when the relic neutralino density is in the bounds previously associated with the so-called flat and accelerating Universe $0.1 < \Omega_\chi h_0^2 < 0.3$. The black triangles in Fig. 11, *b, d* correspond to imposing the WMAP [1, 2] constraint on matter relic density $0.094 < \Omega_\chi h_0^2 < 0.129$. Despite a visible reduction of the allowed domain for the relic density due to the WMAP result, the upper bounds for the spin-dependent and spin-independent WIMP–nucleon cross sections are not significantly affected. From the comparison of circle and square distributions, as expected, follows that the largest cross-section values correspond to the smallest values of the Ω_χ , especially for smaller LSP masses. It is seen that the LSP as a subdominant DM particle favors the large SD and SI cross sections. Furthermore, the maximal SD and SI cross sections in Fig. 11 come for very small relic density values $0.0 < \Omega_\chi h^2 < 0.002$.

One can see also that in our effMSSM with parameters from (30) the lower bound value in the relic density constraints (as, for example, 0.094 in the case of WMAP) restricts from below the allowed masses of the LSP in accordance with the previous considerations [22, 48].

The spin-dependent and spin-independent WIMP–proton cross sections as functions of input MSSM parameters μ , M_A , $\tan \beta$, and $m_{\tilde{Q}}^2$ from the WIMP low-mass set (30) one can find in [70]. They are relevant WIMP low-mass updated modifications of scatter plots given in Figs. 9 and 10.

From these figures one can see the similarity of the scatter plots for spin-dependent and scalar cross sections as functions of μ and $m_{\tilde{Q}}^2$. The decrease of both lower bounds of the cross sections with $m_{\tilde{Q}}^2$ occurs due to the increase of masses of squarks, which enter the s-channel intermediate states. Both spin-dependent and spin-independent cross sections increase when $|\mu|$ decreases, in agreement with literature [80, 99, 100] and our previous calculations [9, 50]. As before, the increase of the scalar cross sections generally is connected with the increase of the Higgsino admixture of the LSP and increase of Higgsino–gaugino interference which enters this cross section [99–101]. The reason of the Higgsino growth can be nonuniversality of scalar soft masses [100], variation of intermediate unification scale [101], or focus point regime of the supersymmetry [99]. There is no any visible sensitivity of the SD cross sections to $\tan \beta$ and M_A (Higgs bosons do not contribute) but the SI cross section possesses remarkable dependence on these parameters. The SI cross sections rather quickly drop with the growth of the *CP*-odd Higgs mass M_A and increase with $\tan \beta$ [49, 50, 86, 100–103]. The different $\tan \beta$ and M_A dependence of the SD and SI cross sections as well as the general about-2-order-of-magnitude excess of the spin-dependent cross sections over spin-independent cross sections may be important for observations [9, 24, 25, 79, 104]. It is interesting to note, that maximal values for the LSP-proton SD cross section one can obtain in the pure Higgsino case (when only *Z* exchange contributes) at a level of $5 \cdot 10^{-2}$ pb.

Finally, it is perhaps the right place to comment the following. Unfortunately, the MSSM parameter space is huge and to obtain some reliable feeling, concerning, for example, the expected rate of dark matter detection when all relevant experimental and cosmological constraints are taken into account, one has nothing but this statistical numerical method (see, for example, [46,48,53–55,86,105,106]). This method allows lower and upper bounds for any observable to be estimated, and to make conclusions about the prospects for dark matter detection with modern or near-future high-accuracy dark matter detectors. The larger the amount of points which confirms such a conclusion the better. The conclusions we made here are based on hundreds of thousand of points which passed all constraints. Of course, we have no proved protection against peculiar choices of parameters which could lead to some cancellation and to small cross sections even if Higgs masses are small. Nevertheless, the probability of these choices is very small (about 1/100000), otherwise we should already meet them with our random scanning. On the other side, if these peculiar choices exist and one-day would manifest themselves, this would be a very interesting puzzle, because it would be some kind of fine tuning of parameters, which requires strong further development of our understanding of the theory [50].

3.2. One Does not Miss a DM Signal Due to the Spin. The above-mentioned difference in $\tan\beta$ and M_A dependence of the SD and SI cross sections as well as the visible low bound for the SD cross sections indeed have important consequences for observations. To be more definite with the statement we present in Fig. 12 a comparison of total spin-dependent versus total spin-independent event rates in ^{73}Ge — as representative and one of the most promising high-spin isotopes for future construction of high-sensitivity detectors. The spin of ^{73}Ge is equal to $9/2$.

Figure 12 shows the weak dependence (increase) of the ratio $R(0, \text{inf})_{\text{SD}}/R(0, \text{inf})_{\text{SI}}$ on mass of the LSP with the mean value being approximately 0.01–0.1. There are very large and very small values for the ratio practically for any given mass of the LSP. The spin-independent (scalar) contribution obviously dominates in the domain of large expected rates in the Germanium detector ($R > 0.1$ events/(kg · day)) as was obtained before (see, for example, [49]). But as soon as the total rate drops down to $R < 0.01$ events/(kg · day), or, equivalently, the scalar neutralino–proton cross section becomes smaller than 10^{-9} – 10^{-10} pb, the spin-dependent interaction may produce a rather non-negligible contribution to the total event rate. Moreover, if the scalar cross section decreases further ($\sigma < 10^{-12}$ pb), it becomes obvious that the spin contribution alone saturates the total rate and protects it (see lower bounds in Figs. 9, 10 and 11) from decreasing below $R \approx 10^{-6}$ – 10^{-7} events/(kg · day) [50]. This observation could be quite important for experiments actually looking for direct *detection* of dark matter, but not only for exclusion plots. Indeed, while scalar cross sections governed mostly by Higgs exchange can be rather small (when

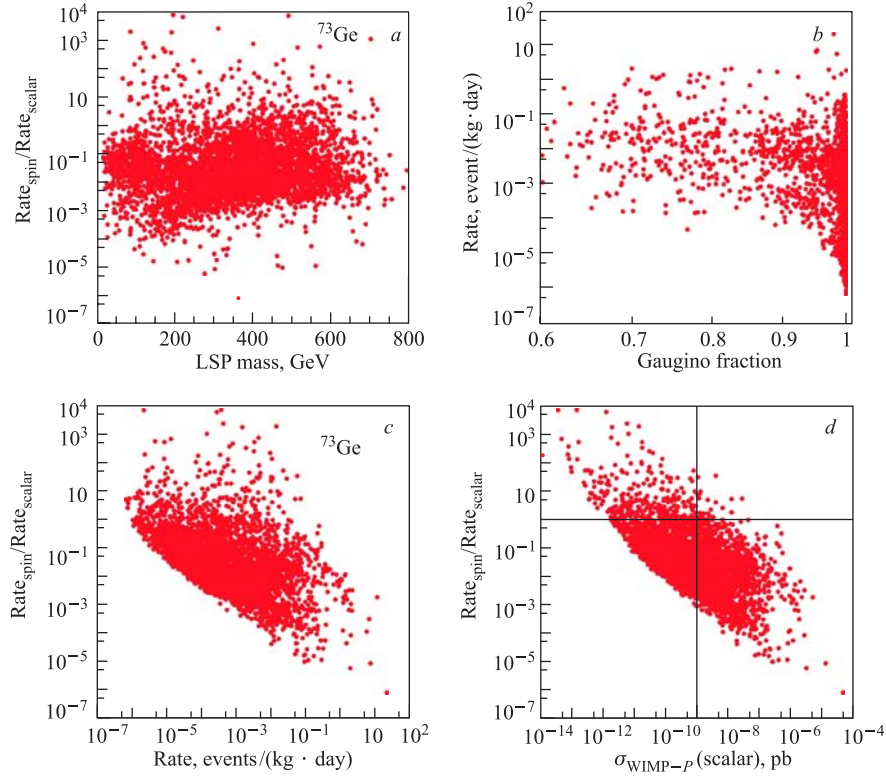


Fig. 12. Ratio of spin-dependent event rate to the spin-independent event rate in ^{73}Ge isotope as a function of LSP mass (*a*), total (spin-dependent plus spin-independent) event rate (*c*) and scalar cross section of neutralino–proton interaction (*d*) obtained with $0.1 < \Omega_\chi h_0^2 < 0.3$. The vertical line gives the best expected sensitivity of the GENIUS project [107–110]. In the region above the horizontal line, the spin contribution dominates. The total event rate versus gaugino fraction of LSP P is also given (*b*). For total rate definitions see (25)

Higgs masses remain large enough, for example, in the Next-to-Minimal Supersymmetric Standard Model [111]) the spin cross section cannot be arbitrary small, because the mass of the Z boson, which gives the dominant contribution, is well defined, provided one ignores any possible fine-tuning cancellations [112].

Therefore, if an experiment with sensitivity 10^{-5} – 10^{-6} event/(kg · day) fails to detect a dark matter signal, an experiment with higher sensitivity should have a nonzero-spin target and will be able to detect dark matter particles only due to the spin neutralino–quark interaction.

4. TWO CONSTRAINTS FOR SUSY DUE TO THE SPIN

From general definitions of SD and SI WIMP–nucleus and WIMP–nucleon cross sections (Eqs. (7)–(12), (14) and (15)) one can conclude that the spin observables in DM search give us two independent constraints on a SUSY model via $\sigma_{\text{SD}}^p(0)$ and $\sigma_{\text{SD}}^n(0)$, or, equivalently, via a_p and a_n . These constraints are usually presented in the form of exclusion curves obtained with different target nuclei and recalculated in terms of $\sigma_{\text{SD}}^p(0)$ (Fig. 13) and $\sigma_{\text{SD}}^n(0)$ (Fig. 14). This presentation is a bit obsolete [7, 58, 70], but it allows one to compare sensitivities

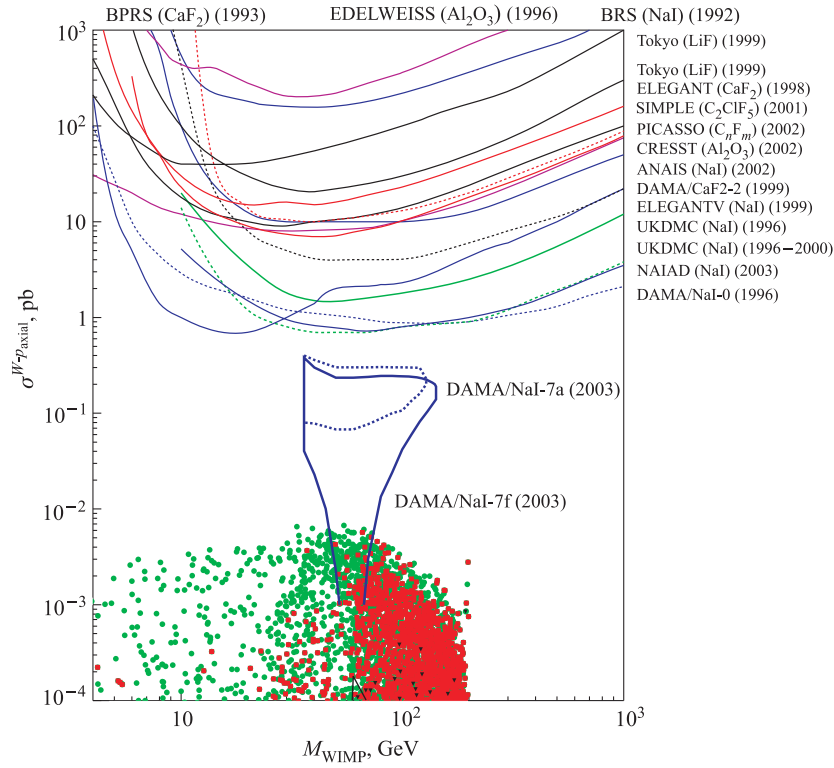


Fig. 13. Exclusion curves for the SD WIMP–proton cross section (σ_{SD}^p versus WIMP mass). The curves are obtained from [113–136]. DAMA/NaI-7a(f) contours for WIMP–proton SD interaction in ^{127}I are obtained on the basis of the positive and model-independent signature of annual signal modulation in the framework of a mixed scalar-spin coupling approach [7, 58]. The scatter plots correspond to our calculations given in Fig. 11. The scattered points are calculations of [70]. The small triangle-like shaded area in the bottom is taken from [137]. Note that the *closed* DAMA contour is above the upper limit for $\sigma_{\text{SD}}^p \approx 5 \cdot 10^{-2}$ pb

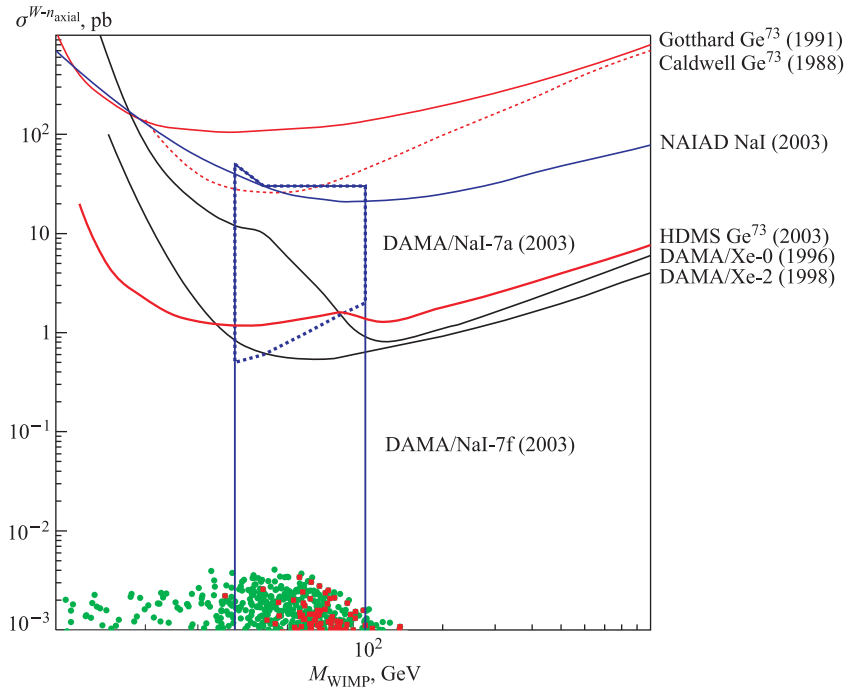


Fig. 14. Exclusion curves for the SD WIMP–neutron cross section (σ_{SD}^n versus WIMP mass). The curves are taken from [19, 136, 138–142]. DAMA/NaI-7a(f) contours for WIMP–neutron SD interaction (subdominating in ^{127}I) are obtained by us from the relevant figures of [7, 58]. The scatter plots correspond to our calculations given in Fig. 11. Note that the NAIAD curve here corresponds to the subdominant for ^{127}I WIMP–neutron SD interaction. The curve was extracted from the nucleus ^{127}I (which has dominating WIMP–proton SD interaction) in the approach of [79]. It is much weaker in comparison with the relevant NAIAD curve for the WIMP–proton SD interaction in Fig. 13

of different experiments. At the current level of accuracy (when $f_q^{(p)} \approx f_q^{(n)}$ and $\sigma_{\text{SI}}^p(0) \approx \sigma_{\text{SI}}^n(0)$, see Fig. 8) there is only one similar constraint (given in Fig. 4) from spin-independent DM search experiments (see Eq. (7)).

Indeed, for the spin-zero nuclear target the experimentally measured event rate (1) of direct DM particle detection, via formula (4) is connected with the zero-momentum WIMP–proton(neutron) cross section (7). The zero-momentum scalar WIMP–proton(neutron) cross section $\sigma_{\text{SI}}^p(0)$ can be expressed through effective neutralino–quark couplings \mathcal{C}_q (13) by means of expression (14). These couplings \mathcal{C}_q (as well as \mathcal{A}_q) can be directly connected with the fundamental parameters of a SUSY model such as $\tan\beta$, $M_{1,2}$, μ , masses of sfermions and Higgs bosons, etc. Therefore experimental limitations on the spin-independent

neutralino–nucleon cross section supply us with a constraint on the fundamental parameters of an underlying SUSY model. In the case of the spin-dependent WIMP–nucleus interaction from a measured differential rate (1) one first extracts a limitation for $\sigma_{\text{SD}}^A(0)$, and therefore has in principle two constraints [23] for the neutralino–proton a_p and neutralino–neutron a_n effective spin couplings, as follows from relation (8). From (8) one can also see that contrary to the spin-independent case (7) there is no, in general, factorization of the nuclear structure for $\sigma_{\text{SD}}^A(0)$. Both proton $\langle \mathbf{S}_p^A \rangle$ and neutron $\langle \mathbf{S}_n^A \rangle$ spin contributions simultaneously enter into formula (8) for the SD WIMP–nucleus cross section $\sigma_{\text{SD}}^A(0)$.

In the earlier considerations based on the OGM [56,64] one assumed that the nuclear spin is carried by the «odd» unpaired group of protons or neutrons and only one of either $\langle \mathbf{S}_n^A \rangle$ or $\langle \mathbf{S}_p^A \rangle$ is nonzero (the same is true in the ISPSM [52, 62,77,78]). In this case all possible target nuclei can naturally be classified into neutron-odd and proton-odd groups.

Following this classification, the experimental situation in the form of the exclusion curves for the spin-dependent WIMP–proton cross section is given in Fig. 13. The data are taken from experiments BRS (NaI, 1992) [113,114], BPRS (CaF₂, 1993) [115], EDELWEISS (sapphire, 1996) [116], DAMA (NAI, 1996) [117], DAMA (CaF₂, 1999) [118,119], UKDMS (NaI, 1996) [120–123], ELEGANT (CaF₂, 1998) [124], ELEGANT (NaI, 1999) [125, 126], Tokio (LiF, 1999, 2002) [127–131], SIMPLE (C₂ClF₅, 2001) [132], CRESST (Al₂O₃, 2002) [133], PICASSO (C_nF_m, 2002) [134], ANAIS (NaI, 2002) [135] and NAIAD (NaI, 2003) [136]. Although the DAMA/NaI-7 (2003) contours [7] are obtained on the basis of the positive and model-independent signature of the annual signal modulation (closed contour) as well as in the mixed coupling framework (open contour) [58] the contours for the WIMP–proton SD interaction are also presented in the figure.

The exclusion curves for the spin-dependent WIMP–neutron cross sections are given in Fig. 14. The data are taken from the first experiments with natural Ge (1988, 1991) [138,139], xenon (DAMA/Xe-0,2) [140–142], sodium iodide (NAIAD) [136], and from the HDMS experiment with a ⁷³Ge target [19]. Similar to Fig. 13, the DAMA/NaI-7 (2003) [7] contours for the WIMP–neutron SD interaction (subdominant in ¹²⁷I) are placed in the figure. In the nearest future one can also expect some exclusion curves for the SD cross section, for example, from the CDMS [143] and EDELWEISS [144] experiments with natural germanium bolometric detectors.

For comparison in Figs. 13 and 14 are also given scatter plots for SD proton and neutron cross sections which correspond to the results of our calculations shown in Fig. 11. From Figs. 13 and 14 one can, in general, conclude that an about two-orders-of-magnitude improvement of the current DM experimental sensitivities (in the form of these exclusion curves) is needed to reach the SUSY

predictions for the $\sigma_{\text{SD}}^{p,n}$, provided the SUSY lightest neutralino is the best WIMP particle candidate.

It is worthing to note that the calculated scatter plots for σ_{SD}^p (Fig. 13) are obtained without any assumption about $\sigma_{\text{SD}}^n = 0$, but the experimental exclusion curves for σ_{SD}^p traditionally were extracted from the data under the full ignoring of the spin-neutron contribution, i.e., under the assumption $\sigma_{\text{SD}}^n = 0$. This *one-spin-coupling dominance scheme* (always used before a new approach was proposed in [79]) gave a bit too pessimistic exclusion curves, but allowed on the same ground the direct comparison of exclusion curves from different nuclear target experiments. More stringent constraints on σ_{SD}^p one obtains following [79] and [6–8] assuming both $\sigma_{\text{SD}}^p \neq 0$ and $\sigma_{\text{SD}}^n \neq 0$, although usually for the proton-odd-like nuclei the contribution of the neutron spin is very small ($\langle \mathbf{S}_n^A \rangle \ll \langle \mathbf{S}_p^A \rangle$). Therefore the direct comparison of old-fashioned exclusion curves with new ones is misleading *in general*. The same conclusion concerns [7, 8] direct comparison of the SI exclusion curves (obtained without any SD contribution) with new SI exclusion curves (obtained with nonzero SD contribution) as well as with the results of the SUSY calculations (Fig. 4). In principle, this observation can resolve the conflict between the DAMA evidence and the results of other DM experiments.

5. MIXED SPIN–SCALAR WIMP–NUCLEON INTERACTIONS

Further more accurate calculations of spin nuclear structure [21, 47, 57, 59, 60, 65, 66, 68, 73, 74, 76] demonstrate that contrary to the simplified odd-group approach both $\langle \mathbf{S}_p^A \rangle$ and $\langle \mathbf{S}_n^A \rangle$ differ from zero, but nevertheless one of these spin quantities always dominates ($\langle \mathbf{S}_p^A \rangle \ll \langle \mathbf{S}_n^A \rangle$, or $\langle \mathbf{S}_n^A \rangle \ll \langle \mathbf{S}_p^A \rangle$). *If together with the dominance like $\langle \mathbf{S}_{p(n)}^A \rangle \ll \langle \mathbf{S}_{n(p)}^A \rangle$ one would have the WIMP–proton and WIMP–neutron couplings of the same order of magnitude (not $a_{n(p)} \ll a_{p(n)}$), the situation could look like that in the odd-group model and one could safely (at the current level of accuracy) neglect subdominant spin contribution in the data analysis (see Eq. (8)).*

Following an analogy between neutrinos and neutralinos, one can assume that neutralino couplings with the neutron and proton should not be very different [145] and one could expect preferably $|a_n|/|a_p| \approx O(1)$. The assumption has been checked in effMSSM approach for large LSP masses in [25, 83] and for relatively low LSP masses $m_\chi < 200 \text{ GeV}/c^2$ in [70]. Figure 15 shows that for the ratio of a_n to a_p we have the bounds

$$0.55 < |a_n/a_p| < 0.8. \quad (31)$$

The scatter plots in Fig. 15 as previously (see Fig. 11) were obtained with the relic neutralino density $0.0 < \Omega_\chi h_0^2 < 1.0$ (circles), with subdominant relic neutralino

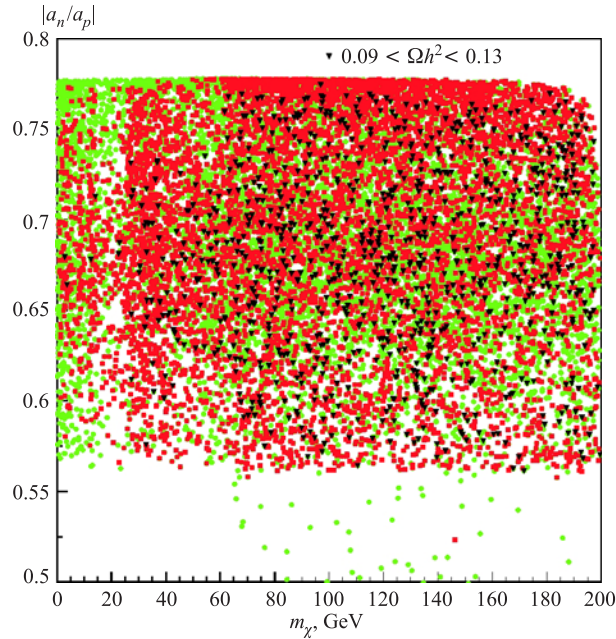


Fig. 15. The scatter plots (circles, squares, and triangles) give the ratio of the neutralino–neutron spin coupling a_n to the neutralino–proton spin coupling a_p in the efmSSM under the notations as in Fig. 11. The ratio is restricted to the range between 0.55 and 0.8

contribution $0.002 < \Omega_\chi h_0^2 < 0.1$ (squares) and with a WMAP-inspired relic neutralino density of $0.094 < \Omega_\chi h_0^2 < 0.129$ (black triangles). Therefore in the model the couplings are almost the same and one can safely neglect, for example, the $\langle \mathbf{S}_p^A \rangle$ -spin contribution in the analysis of the DM data for a nuclear target with $\langle \mathbf{S}_p^A \rangle \ll \langle \mathbf{S}_n^A \rangle$.

Furthermore, when one compares in the same figure an exclusion curve for SD WIMP–proton coupling obtained without subdominant SD WIMP–neutron contribution and without SI contribution (all curves in Fig. 13 except the one for NAIAD [136] and one for Tokyo-LiF [131]) with a curve from the approach of [79], when the subdominant contribution is included (the NAIAD and Tokyo-LiF curves in Fig. 13), one «artificially» improves the sensitivity of the *latter* curves (NAIAD or Tokyo-LiF) in comparison with the former ones. To be consistent and for reliable comparisons, one should coherently recalculate all previous curves in the new manner. This message is also stressed in [7]. The same arguments are true for the last results of the SIMPLE experiment [146] and search for DM with NaF bolometers [147] where the SI contribution seems

also completely ignored. Although ^{19}F has the best properties for investigation of WIMP–nucleon spin-dependent interactions (see, for example, [47]) it is not obvious that one should completely ignore spin-independent WIMP coupling with the fluorine. At least, for isotopes with atomic number $A > 50$ [46, 49] the ignoring of the SI contribution would be a larger mistake than the neglect of the subdominant SD WIMP–neutron contribution, when the SD WIMP–proton interaction dominates. Therefore we would like to note that the «old» odd-group-based approach in analyzing the SD data from experiments with heavy enough targets (for example, germanium) is still quite suitable. Especially when it is not obvious that (both) spin couplings dominate over the scalar one.

From measurements with ^{73}Ge one can extract, in principle, not only the dominant constraint for WIMP–nucleon coupling a_n (or σ_{SD}^n) but also the constraint for the subdominant WIMP–proton coupling a_p (or σ_{SD}^p) using the approach of [79]. Nevertheless, the latter constraint will be much weaker in comparison with the constraints from p -odd group nuclear targets, like ^{19}F or I. This fact is illustrated by the NAIAD (NaI, 2003) curve in Fig. 14, which corresponds to the subdominant WIMP–neutron spin contribution extracted from the p -odd nucleus I.

Another approach of Bernabei et al. [58] looks in a more appropriate way for the mixed spin–scalar coupling data presentation, and is based on an introduction of the so-called effective SD nucleon cross section $\sigma_{\text{SD}}^m(0)$ (originally σ_{SD} in [7, 58]) and coupling mixing angle θ (11) instead of $\sigma_{\text{SD}}^p(0)$ and $\sigma_{\text{SD}}^n(0)$. With these definitions the SD WIMP–proton and WIMP–neutron cross sections are given by relations (12).

In Fig. 16 the WIMP–nucleon spin and scalar mixed couplings allowed by the annual modulation signature from the 100-kg DAMA/NaI experiment are shown inside the shaded regions. The regions from [7, 58] in the $(\xi\sigma_{\text{SI}}, \xi\sigma_{\text{SD}})$ space for $40 < m_{\text{WIMP}} < 110$ GeV cover spin–scalar mixing coupling for the proton ($\theta = 0$ case of [7, 58], Fig. 16, *a*) and spin–scalar mixing coupling for the neutron ($\theta = \pi/2$, Fig. 16, *b*). From nuclear physics one has for the proton spin dominated ^{23}Na and ^{127}I $\langle \mathbf{S}_n \rangle / \langle \mathbf{S}_p \rangle < 0.1$ and $\langle \mathbf{S}_n \rangle / \langle \mathbf{S}_p \rangle < 0.02\text{--}0.23$, respectively. For the $\theta = 0$ due to the p -oddness of the I target, the DAMA WIMP–proton spin constraint is the most severe one (see Fig. 13).

In the right panel of Fig. 16 we present the exclusion curve (dashed line) for the WIMP–proton spin coupling from the proton-odd isotope ^{129}Xe obtained under the mixed coupling assumptions [58] from the DAMA-LiXe (1998) experiment [142, 148, 149]. For the DAMA NaI detector the $\theta = \pi/2$ means no $\langle \mathbf{S}_p \rangle$ contribution at all. Therefore, in this case DAMA gives the subdominant $\langle \mathbf{S}_n \rangle$ contribution only, which could be compared further with the dominant $\langle \mathbf{S}_n \rangle$ contribution in ^{73}Ge .

The scatter plots in Fig. 16 give σ_{SI}^p as a function of σ_{SD}^p (*a*) and σ_{SD}^n (*b*) calculated in [70] with parameters from (30) under the same constraints on the relic neutralino density as in Fig. 11. Filled circles correspond to relic neutralino

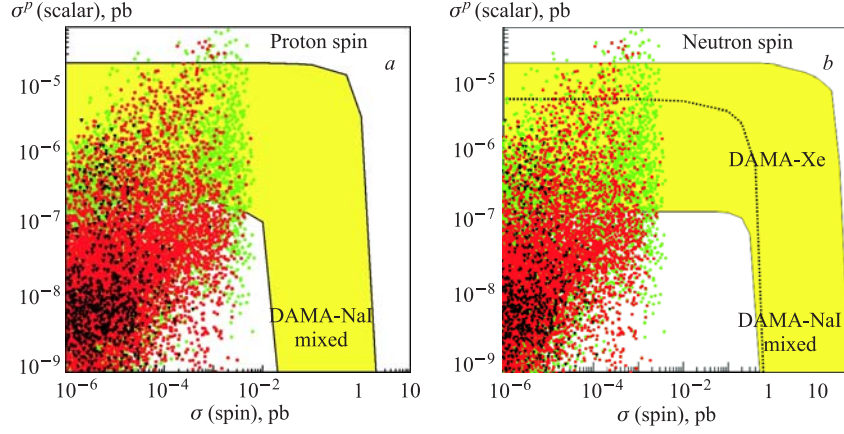


Fig. 16. The DAMA-NaI region from the WIMP annual modulation signature in the $(\xi\sigma_{\text{SI}}, \xi\sigma_{\text{SD}})$ space for $40 < m_{\text{WIMP}} < 110$ GeV [7, 58]. Figure *a* corresponds to dominating (in ^{127}I) SD proton coupling only ($\theta = 0$) and Fig. *b* corresponds to subdominating SD neutron coupling only ($\theta = \pi/2$). The scatter plots give correlations between σ_{SI}^p and σ_{SD} in the effMSSM ($\xi = 1$ is assumed) for $m_\chi < 200$ GeV under the same notations as in Fig. 11. In Fig. *b* the DAMA liquid xenon exclusion curve from [58] is given (dashed line)

density $0.0 < \Omega_\chi h_0^2 < 1.0$, squares correspond to subdominant relic neutralino contribution $0.002 < \Omega_\chi h_0^2 < 0.1$, and black triangles correspond to WMAP density constraint $0.094 < \Omega_\chi h_0^2 < 0.129$.

The constraints on the SUSY parameter space in the mixed coupling framework in Fig. 16 are, in general, much stronger in comparison with the traditional approach based on the one-coupling dominance (Figs. 4, 13 and 14).

It follows from Fig. 16, that when the LSP is the subdominant DM particle (squares in the figure), SD WIMP–proton and WIMP–neutron cross sections at a level of $(3-5) \cdot 10^{-3}$ pb are allowed, but the WMAP relic density constraint (triangles) together with the DAMA restrictions leaves only $\sigma_{\text{SD}}^{p,n} < 3 \cdot 10^{-5}$ pb without any visible reduction of allowed values for σ_{SI}^p . In general, according to the DAMA restrictions, small SI cross sections are completely excluded, only $\sigma_{\text{SI}}^p > (3-5) \cdot 10^{-7}$ pb are allowed. Concerning the SD cross section the situation is not clear, because for the allowed values of the SI contribution, the SD DAMA sensitivity did not yet reach the calculated upper bound for the SD LSP–proton cross section of $5 \cdot 10^{-2}$ pb.

In general, the famous DAMA conflict with other (negative) DM results from CDMS and EDELWEISS experiments can be safely bypassed on the basis of the above-mentioned mixed spin–scalar coupling approach, where both SD and SI couplings are considered simultaneously non-negligible.

5.1. The Mixed Couplings Case for the High-Spin ^{73}Ge . Comparing the number of exclusion curves in Figs. 13 and 14 one can see that there are many measurements with p -odd nuclei and there is a lack of data for n -odd nuclei, i.e., for σ_{SD}^n . Therefore measurements with n -odd nuclei are needed. From our point of view, this lack of σ_{SD}^n measurements can be filled with new data expected from the HDMS experiment with the high-spin isotope ^{73}Ge [19]. This isotope looks with a good accuracy like an almost pure n -odd group nucleus with $\langle \mathbf{S}_n \rangle \gg \langle \mathbf{S}_p \rangle$ (Table 2). The variation of the $\langle \mathbf{S}_p \rangle$ and $\langle \mathbf{S}_n \rangle$ in Table 2 reflects the level of inaccuracy and complexity of the current nuclear structure calculations.

In the mixed spin–scalar coupling approach to estimate the direct detection rate for ^{73}Ge one can use formulas (25). The subdominant contribution from WIMP–proton spin coupling proportional to $\langle \mathbf{S}_p^A \rangle$ can be safely neglected for ^{73}Ge . We consider only a simple spherically symmetric isothermal WIMP velocity distribution [78, 150] and do not go into details of any possible and in principle important uncertainties (and/or modulation effects) of the Galactic halo WIMP distribution [44, 151–156]. For simplicity we use the Gaussian scalar and spin nuclear form factors from [63, 157]. We perform below a simple estimation of prospects for DM search and SUSY constraints with the high-spin ^{73}Ge detector HDMS assuming mixing of WIMP–neutron spin and WIMP–nucleon scalar couplings together with available results from the DAMA-NaI and LiXe experiments [6–8, 142, 148, 149].

The Heidelberg Dark Matter Search (HDMS) experiment uses a special configuration of two Ge detectors to efficiently reduce the background [19, 158]. From the first preliminary results of the HDMS experiment with inner HPGe crystal of enriched ^{73}Ge [19] we can estimate the current background event rate $R(\epsilon, \varepsilon)$ integrated here from the «threshold» energy $\epsilon = 15$ keV to «maximal» energy $\varepsilon = 50$ keV. We obtain $R(15, 50) \approx 10$ events/(kg · day). A substantial improvement of the background (up to an order of magnitude) is further expected for the setup in the Gran Sasso Underground Laboratory. In Fig. 17, solid lines for the integrated rate $R(15, 50)$ marked with numbers 10, 1.0 and 0.1 (in events/(kg · day)) present for $m_{\text{WIMP}} = 70$ GeV our exclusion curves expected from the HDMS setup with ^{73}Ge in the framework of mixed SD WIMP–neutron and SI WIMP–nucleon couplings. Unfortunately, the current background index for HDMS is not yet optimized, and the relevant exclusion curve (marked with 10 events/(kg · day)) has almost the same strength to reduce σ_{SD}^n as the dashed curve from the DAMA experiment with liquid Xe [58] obtained for $m_{\text{WIMP}} = 50$ GeV (better sensitivity is expected with HDMS for $m_{\text{WIMP}} < 40$ GeV). However, both experiments lead already to some sharper restriction for σ_{SD}^n than obtained by DAMA (see Fig. 17). One-order-of-magnitude improvement of the HDMS sensitivity (curve marked with 1.0) will supply us with the best exclusion curve for SD WIMP–neutron coupling, but this sensitivity is not yet enough to reach the calculated upper bound for σ_{SD}^n . This sensitivity also could reduce the upper bound for SI

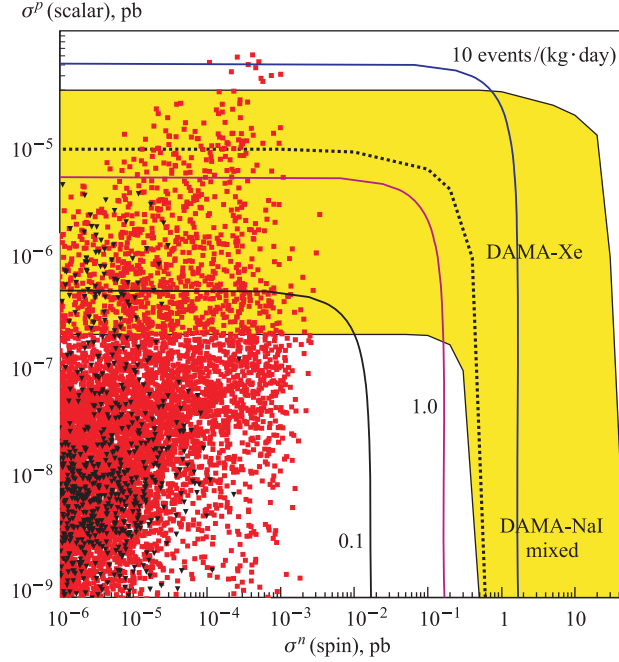


Fig. 17. The solid lines (marked with numbers of $R(15, 50)$ in events/(kg·day) show the sensitivities of the HDMS setup with ^{73}Ge in the framework of mixed SD WIMP–neutron and SI WIMP–nucleon couplings. The DAMA-NaI region for subdominant SD WIMP–neutron coupling ($\theta = \pi/2$) is from Fig. 16. Scatter plots give correlations between σ_{SI}^p and σ_{SD}^n in the effMSSM for $m_\chi < 200$ GeV. The squares correspond to subdominant relic neutralino contribution $0.002 < \Omega_\chi h_0^2 < 0.1$ and black triangles correspond to WMAP relic neutralino density $0.094 < \Omega_\chi h_0^2 < 0.129$. The dashed line from [58] shows the DAMA-LiXe (1998) exclusion curve for $m_{\text{WIMP}} = 50$ GeV

WIMP–proton coupling σ_{SI}^p to a level of 10^{-5} pb. Nevertheless, only an *additional* about-one-order-of-magnitude HDMS sensitivity improvement is needed to obtain decisive constraints on σ_{SI}^p as well as on σ_{SD}^n . In this case only quite narrow bounds for these cross sections will be allowed (below the curve marked by 0.1 and above the lower bound of DAMA-NaI mixed region).

6. SOME OTHER CONSEQUENCES OF THE DAMA RESULTS

It follows from Figs. 4, 13, 14, and 16 that the main results of the DAMA experiment one could summarize in the limitations of the WIMP mass, and the restrictions on the cross section of the *scalar* WIMP–proton interaction. Quite

approximately (having in mind all possible uncertainties of [7,8]) one can write them in the form:

$$40 < m_{\text{WIMP}} < 150 \text{ GeV}, \quad 1 \cdot 10^{-7} < \sigma_{\text{SI}}^p(0) < 3 \cdot 10^{-5} \text{ pb}. \quad (32)$$

The limitations of (32) should have some consequence for observables. Taking them into account we have obtained the reduction of our scatter plots for the total expected event rate of direct WIMP detection in a ^{73}Ge detector (Fig. 18) and the

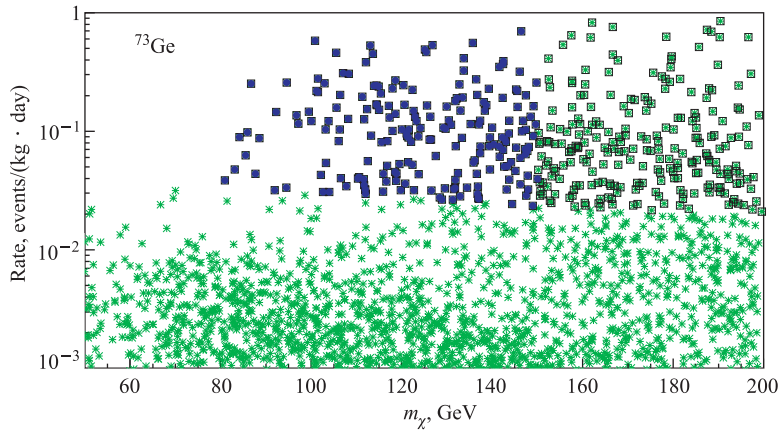


Fig. 18. Event rate for direct neutralino detection in a ^{73}Ge detector as a function of the LSP neutralino mass. Crosses present our calculations with relic density constraint $0.1 < \Omega_\chi h_0^2 < 0.3$ only. Open boxes correspond to implementation of the SI cross-section limit $1 \cdot 10^{-7} < \sigma_{\text{SI}}^p(0) < 3 \cdot 10^{-5}$ pb only, and closed boxes show results with the additional WIMP-mass constraint $40 < m_{\text{WIMP}} < 150$ GeV (see (32))

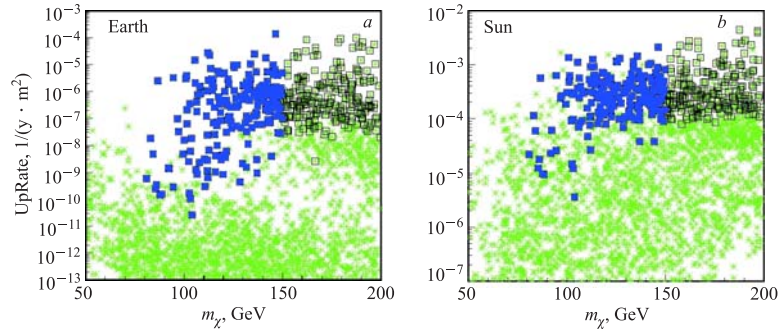


Fig. 19. Indirect detection rate for upgoing muons from DM particles (neutralinos) annihilation in the Earth (a) and the Sun (b) as a function of the LSP neutralino mass. Crosses present our calculations with relic density constraint $0.1 < \Omega_\chi h_0^2 < 0.3$ only. Open boxes correspond to implementation of the SI cross-section limits of (32) only and closed boxes depict results with both limitations of (32)

indirect detection rate for upgoing muons from dark matter particles annihilation in the Earth and the Sun (Fig. 19). The calculations of indirect detection rates follow the description given in [46, 95]. There is also a reduction of allowed masses of some SUSY particles (Fig. 20). In total from these figures one can see that the DAMA evidence favors the light Higgs sector of the MSSM, relatively high event rate in Ge detectors, as well as relatively high upgoing muon fluxes from the Earth and from the Sun for indirect detection of the relic neutralino. It is also

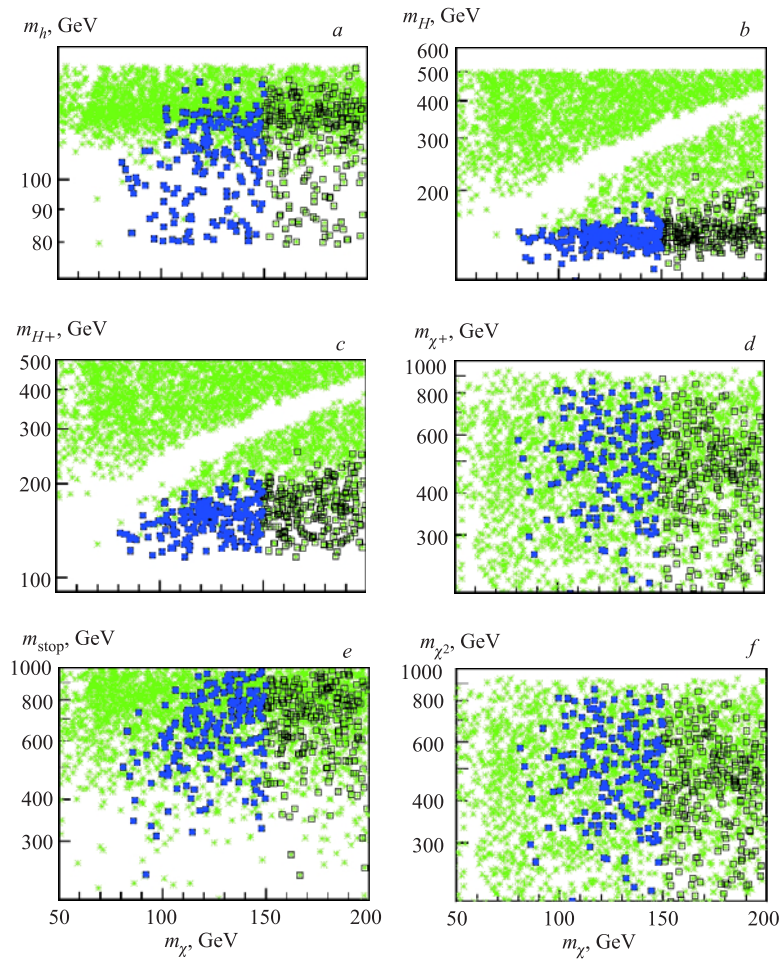


Fig. 20. Masses in GeV of light (m_h) (a), heavy (m_H) (b), and charged Higgs bosons (m_{H^+}) (c), as well as masses of chargino (m_{χ^+}) (d), stop (m_{stop}) (e), and second neutralino (m_{χ_2}) (f), versus the mass (m_{χ_1}) of the LSP neutralino under the same DAMA-inspired restrictions as in Figs. 18, 19

almost insensitive to the sfermion and neutralino–chargino particle masses. As noted before in [50,95], the relatively light Higgs masses (smaller than 200 GeV) are very interesting from the point of accelerator SUSY searches.

In [70], the estimations of the ideal total expected rate $R(0, \text{inf})$ for WIMPs with $M_{\text{WIMP}} < 200 \text{ GeV}/c^2$ in a ^{73}Ge detector are obtained within the effMSSM. In [20], with σ_{SD} and σ_{SI} already calculated in [70], new estimates of the integrated event rate $R(\epsilon, \epsilon)$ for WIMP masses smaller than $200 \text{ GeV}/c^2$ are obtained for a number of other DM targets. For definiteness, the recoil energy threshold $\epsilon = 5 \text{ keV}$ (and sometimes $\epsilon = 10 \text{ keV}$) with the maximal energy $\epsilon = 50 \text{ keV}$ are used. The calculated event rates $R(5, 50)$ and the rate ratios for different targets are depicted as scatter plots in Figs. 21–24. For example, in Fig. 21 one can see total, $R(5, 50)$, spin-independent, $R(5, 50)_{\text{SI}}$, and spin-dependent, $R(5, 50)_{\text{SD}}$, event rates expected in ^{73}Ge target together with their ratio $R(5, 50)_{\text{SD}}/R(5, 50)_{\text{SI}}$ as functions of the WIMP mass. It is always interesting to trace some interplay between SD and SI contributions to the total event rate. To this end, correlations between the total rate $R(5, 50)$ and its SD fraction as well as correlations between the total rate $R(5, 50)$ and the SD-to-SI ratio $R(5, 50)_{\text{SD}}/R(5, 50)_{\text{SI}}$ are

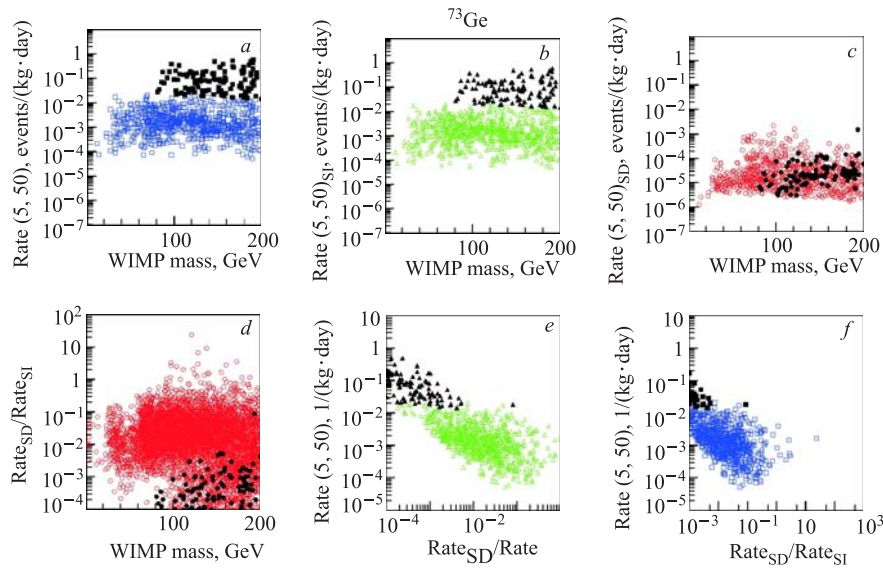


Fig. 21. Expected in ^{73}Ge total $R(5, 50)$, SI and SD event rates $R(5, 50)_{\text{SI}}$ and $R(5, 50)_{\text{SD}}$ (a–c) as well as the ratio $R(5, 50)_{\text{SD}}/R(5, 50)_{\text{SI}}$ (d) as functions of WIMP mass. Correlations between the total rate $R(5, 50)$ and the SD fraction in $R(5, 50)$ are given in the plot e. Correlations between the total rate $R(5, 50)$ and the ratio $R(5, 50)_{\text{SD}}/R(5, 50)_{\text{SI}}$ are given in the plot f. Open symbols correspond to the WMAP constraint $0.094 < \Omega_{\chi} h^2 < 0.129$; closed symbols give rates with an extra DAMA constraint $1 \cdot 10^{-7} < \sigma_{\text{SI}}^p < 3 \cdot 10^{-5} \text{ pb}$

also given in Fig. 21. All open symbols in the figures correspond to the case when the WMAP constraint on the relic neutralino density $0.094 < \Omega_\chi h^2 < 0.129$ is taken into account. The relevant filled symbols show the rates which one would expect if an extra DAMA constraint, $1 \cdot 10^{-7} < \sigma_{\text{SI}}^p < 3 \cdot 10^{-5}$ pb, is imposed on SI cross sections. It is seen that in the last case (filled symbols) the SI rates are at least two orders of magnitude larger than the SD one and the large total rate values ($R > 0.01$ events/(kg · day)) are saturated only by the SI interactions. If one ignores these filled symbols (i.e., the DAMA-inspired extra constraint $1 \cdot 10^{-7} < \sigma_{\text{SI}}^p < 3 \cdot 10^{-5}$ pb), then the SD contribution does not look very suppressed and the SD contribution alone can saturate the total event rate, but only when the rate itself is rather small ($R \approx 0.001$ events/(kg · day)). These features take place for all heavy enough targets, therefore the corresponding figures for NaI, CsI, and Xe target are not given.

It is well known that a fluorine-containing target is the best one for detection and measurement of the spin-dependent WIMP–nucleus interaction (see, e.g., [46, 47]). Figure 22 shows that the SD rate in CF_4 is indeed the biggest one and for a large number of points (MSSM models) the SD contribution dominates. Nevertheless, it is also seen that it is not correct to completely ignore the SI contribution to the total expected rate in the fluorine target [27, 70] because the SI rate is almost the same as the SD one. Furthermore, at a current level of the DM detector sensitivity, when the DAMA-inspired large SI contributions are not

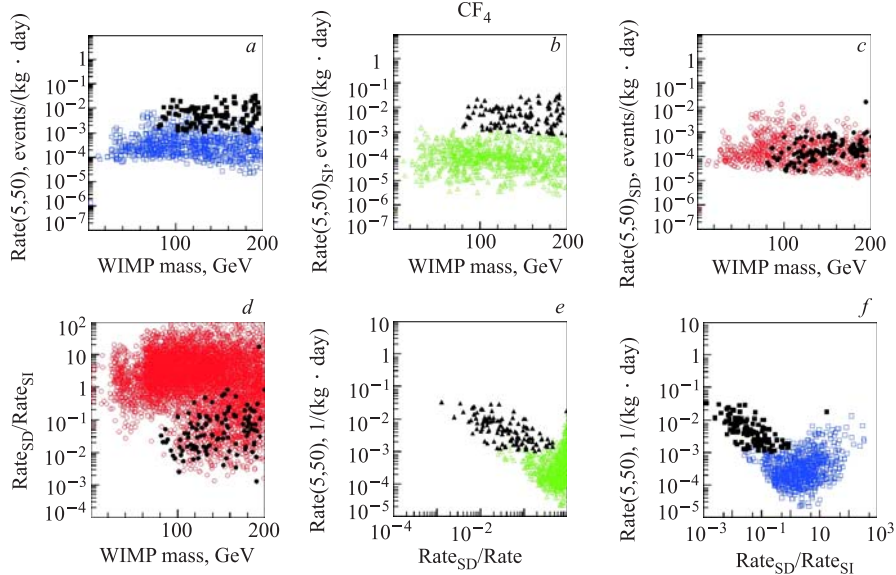


Fig. 22. The same as in Fig. 21, but for CF_4

yet completely excluded (filled symbols in Fig. 22), the SD contribution in CF_4 , $R(5, 50)_{\text{SD}}$, is smaller than the SI one, $R(5, 50)_{\text{SI}}$. The ratios of the total, SI and SD rates in the CF_4 and ^{73}Ge targets are presented in Fig. 23 as a function of WIMP mass.

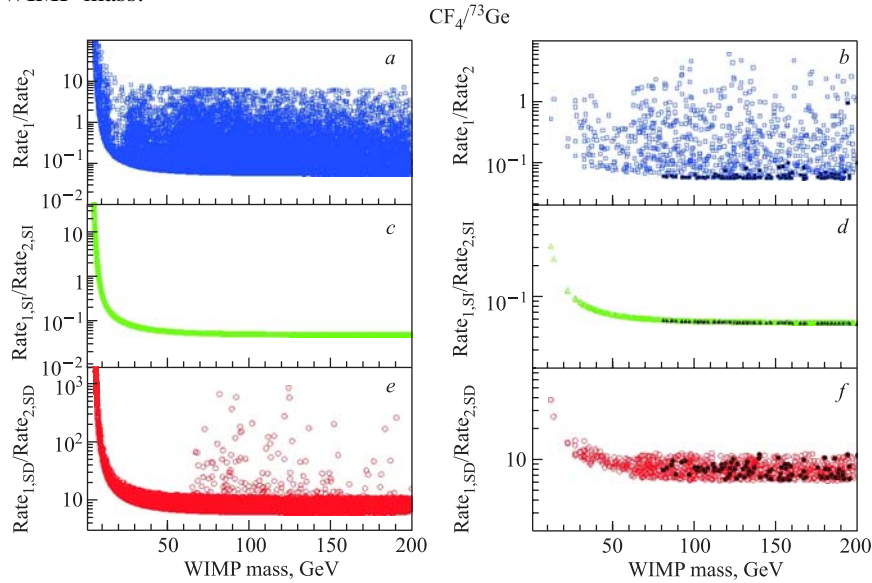


Fig. 23. Ratios $R(5, 50)_{\text{CF}_4}/R(5, 50)_{^{73}\text{Ge}}$ of the total (*a, b*), SI (*c, d*) and SD (*e, f*) rates as functions of WIMP mass. No relic density constraint is imposed in *a, c, e*. Open symbols in *b, d, f* correspond to the WMAP constraint $0.094 < \Omega_\chi h^2 < 0.129$. Filled symbols give these ratios for the rates obtained with an extra DAMA SI constraint, $1 \cdot 10^{-7} < \sigma_{\text{SI}}^p < 3 \cdot 10^{-5}$ pb

The ratios in Fig. 23, *a, c, e* correspond to the rates calculated without any constraint on the relic density of neutralinos in the effMSSM. The increase of these ratios at very low WIMP masses reflects better sensitivity of fluorine to smaller WIMP masses than that of germanium. Open symbols in Fig. 23, *b, d, f* depict these ratios when the WMAP constraint $0.094 < \Omega_\chi h^2 < 0.129$ is imposed on the calculated neutralino relic density. Filled symbols give these ratios for the rates obtained with an extra DAMA SI constraint, $1 \cdot 10^{-7} < \sigma_{\text{SI}}^p < 3 \cdot 10^{-5}$ pb. The sensitivity of CF_4 to the SD WIMP interaction is about ten times as large as the SD sensitivity of ^{73}Ge . At the same time, the CF_4 sensitivity to the SI WIMP interaction is less than 0.1–0.05 of the SI sensitivity of ^{73}Ge . As a result, the total expected rate in ^{73}Ge is a bit larger than in a very spin-sensitive CF_4 target. Figure 23, *b, d, f* shows that the relic density WMAP and extra DAMA constraints make this conclusion stricter. The expected total rate in a heavy enough ^{73}Ge target is about ten times as large as the total expected rate in the CF_4 target.

Absolute values of the total, SD, and SI rates in light-mass targets like CH_4 and ^3He are considerably smaller than in the fluorine-containing CF_4 and germanium targets, especially when the extra WMAP (a, c, e) and DAMA (filled symbols) constraints are imposed. More details one can find in [20].

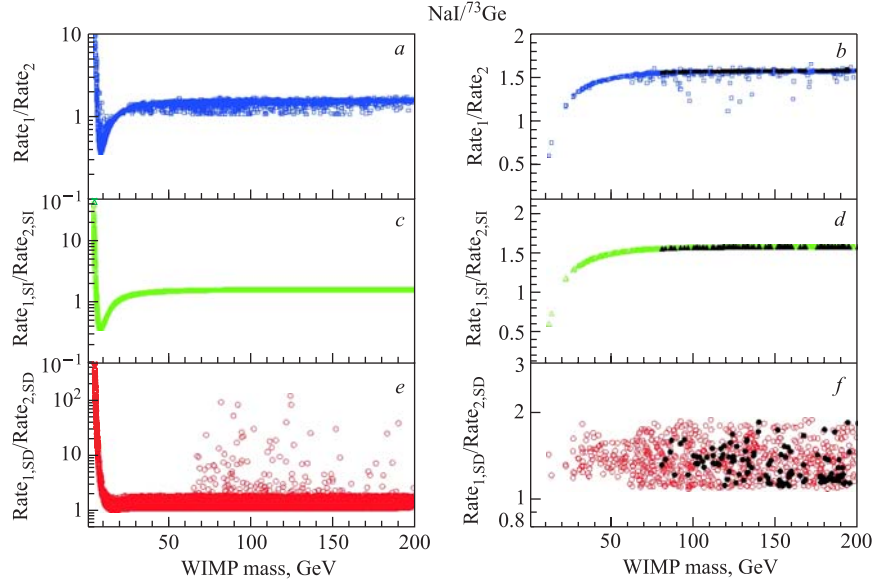


Fig. 24. The same as in Fig. 23, but for NaI and ^{73}Ge

For all detectors with heavy enough target mass (NaI, CsI, Xe, etc.) the absolute values of the total, SI and SD rates look very similar with the only possible exception in the domain of very low-mass WIMPs (when a target contains some light isotope like, for example, Na in the NaI target). In Figure 24 a set of NaI-to- ^{73}Ge rate ratios, $R(5, 50)_{\text{NaI}}/R(5, 50)_{^{73}\text{Ge}}$, is given for illustration of the behavior. All depicted ratios are of the order of unity. Only for very low WIMP masses (less than $10 \text{ GeV}/c^2$) and with the WMAP constraint neglected, the rates in NaI start to clearly dominate over the rates in ^{73}Ge due to kinematically preferable WIMP interaction with Na. This low-WIMP-mass growth of the ratios is absent in the CsI and Xe targets. Furthermore, for these materials the rates in ^{73}Ge dominate in the low-mass WIMP region.

The WIMP–nucleon σ_{SD} and σ_{SI} cross sections which enter event rate (25) were taken above from theoretical calculations in the effMSSM [70]. Another source of these cross sections is, for example, the DAMA experiment [7]. With formulas (1)–(25) the DAMA(NaI) constraints on σ_{SD} and σ_{SI} from [7] can be phenomenologically transformed into the allowed regions for the detection rates

with other targets. The results of these recalculations are given in Figs. 25–27 for the total, SI and SD expected rates $R(10, 50)$ in a number of representative materials for a DM detector. Here the threshold of 10 keV is used. The values of the expected rate can vary within the columns without any conflict with the DAMA-allowed σ_{SD} and σ_{SI} regions. The left (right) parts of these figures contain rate restrictions for the odd-neutron (odd-proton) group model nonzero-spin nuclei (see, e.g., [26]). Some of the highest rate values, for example in ^{73}Ge , are already excluded by measurements [38]. In particular, from Figs. 25–27 one can see that all fluorine-containing targets (LiF , CF_4 , C_2F_6 , and CaF_2 , etc.) have almost the same sensitivity to both the SD and SI WIMP–nucleus interactions. Among all materials considered a detector with a ^{73}Ge , ^{129}Xe , or NaI target has better prospects to confirm or to reject the DAMA result due to the largest values of the lower bounds for the total rate ($R(10, 50) > 0.06\text{--}0.08$ events/(kg · day)). If, for example, one ignores the SI WIMP interaction (Fig. 26), then all materials have almost the same prospects to detect DM particles with the only exception of CH_4 .

The results obtained are based on previous evaluations of the neutralino–proton (neutron) spin and scalar cross sections for the neutralino masses $m_\chi < 200 \text{ GeV}/c^2$ [70].

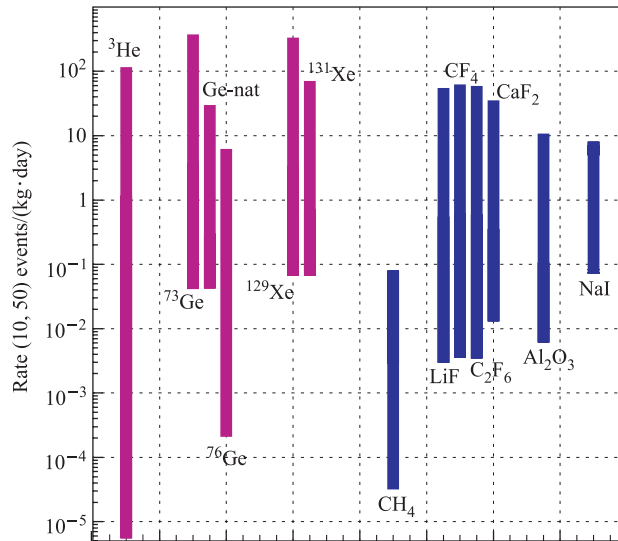


Fig. 25. Variations of expected event rates, $R(5, 50)$, for a number of targets followed from the DAMA-allowed cross sections σ_{SD} and σ_{SI} . Targets with nonzero-spin nuclei from the odd-neutron (odd-proton) group model are given in the left (right) part of the figure

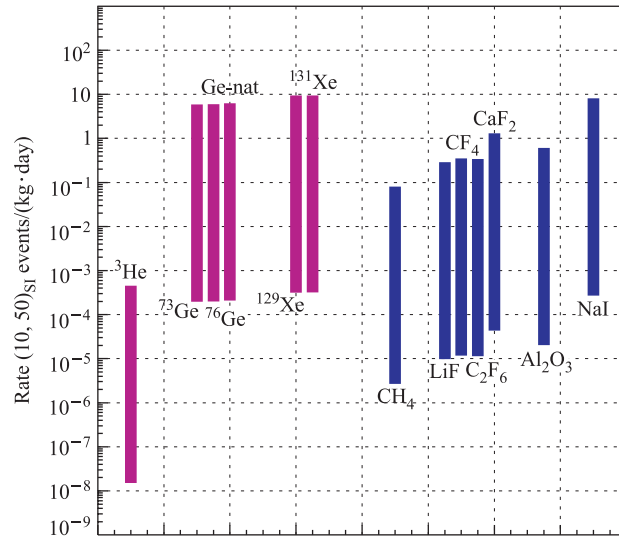


Fig. 26. Variations of expected spin-independent contributions to the event rate, $R(5, 50)_{SI}$, in a number of targets followed from the DAMA-allowed cross sections σ_{SD} and σ_{SI}

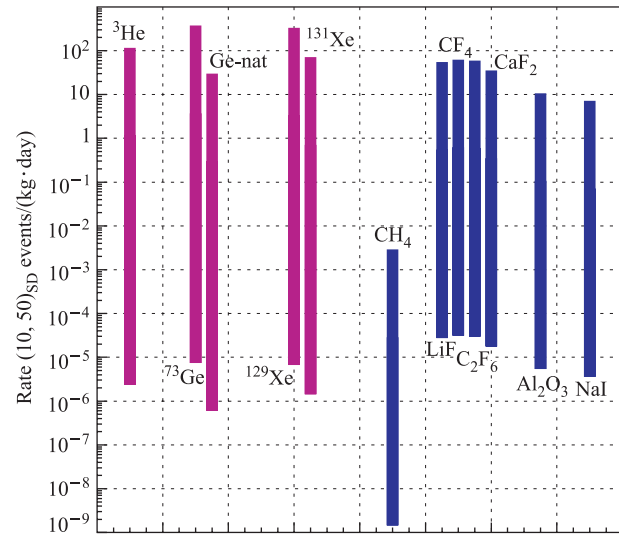


Fig. 27. The same as in Fig. 26, but for the spin-dependent contributions $R(5, 50)_{SD}$

It is worth noting, that to get very accurate predictions for the event rate one has to take into account a number of quite uncertain astrophysical and nuclear parameters and specific features of a real setup. We considered only a simple spherically symmetric isothermal WIMP velocity distribution [78, 150] and do not go into detail of any possible and in principle important uncertainties (and/or modulation effects) of the Galactic halo WIMP distribution [44, 151–156]. For simplicity we use the Gaussian scalar and spin nuclear form factors from [63, 157]. We believe it is relevant for our comparative study because the very influence of the factors is suppressed in the rate ratios.

CONCLUSION

There is continuous theoretical and experimental interest in existence of the cold dark matter of the Universe in the form of the weakly interacting massive particles (WIMPs). One of the best motivated nonbaryonic WIMP dark matter candidates is the neutralino, the lightest supersymmetric particle. The motivation for supersymmetry arises naturally in modern theories of particle physics.

To estimate the expected direct detection rate for these WIMPs, an effective low-energy minimal supersymmetric extension of the Standard Model (effMSSM) is used. The WIMP–proton and WIMP–neutron spin and scalar cross sections at zero-momentum transfer ($\sigma_{SD}^{p,n}(0)$ and $\sigma_{SI}^{p,n}(0)$) were calculated for the rather large WIMP masses as well as in the low WIMP mass regime, which follows from the DAMA dark matter evidence.

There are some reasons to think that spin-dependent interaction of the DM WIMPs with nuclei could be very important. First, contrary to the only one constraint for SUSY models available from the spin-independent WIMP–nucleus interaction, the SD WIMP–nucleus interaction supplies us with two such constraints. Second, for heavy target nuclei and heavy WIMP masses the SD efficiency to detect a DM signal is much higher than the SI efficiency. Third, the absolute lower bound for the DM detection rate can naturally be due to SD interaction. An experiment aimed at *detecting* DM with sensitivity higher than 10^{-5} event/(kg · day) should have a nonzero-spin target. Finally, due to the spin, the DAMA conflict with other DM results can be bypassed in the mixed spin–scalar coupling approach, where both SD and SI couplings are considered simultaneously non-negligible.

We noted a possible incorrectness in the direct comparison of exclusion curves for WIMP–proton(neutron) spin-dependent cross section obtained with and without nonzero WIMP–neutron(proton) spin-dependent contribution. On the other hand, nuclear spin structure calculations show that usually one, WIMP–proton $\langle \mathbf{S}_p^A \rangle$, or WIMP–neutron $\langle \mathbf{S}_n^A \rangle$, nuclear spin dominates and in the effMSSM we have the WIMP–proton and WIMP–neutron effective couplings a_n and a_p of

the same order of magnitude (Fig. 15). Therefore at the current level of accuracy it looks reasonable to safely neglect subdominant WIMP–nucleon contributions analyzing the data from spin-nonzero targets. Furthermore the above-mentioned incorrectness concerns also the direct comparison of spin-dependent exclusion curves obtained with and without nonzero spin-independent contributions [7, 8]. To be consistent, for this comparison one has to use a mixed spin–scalar coupling approach (Figs. 16 and 17), as for the first time proposed by the DAMA collaboration [6–8]. We applied such spin–scalar coupling approach to estimate future prospects of the HDMS experiment with the neutron-odd group high-spin isotope ^{73}Ge . Although the odd-neutron nuclei ^{73}Ge , ^{129}Xe already with the present accuracy lead to some sharper restrictions for σ_{SD}^n than obtained by DAMA, we found that the current accuracy of measurements with ^{73}Ge (as well as with ^{129}Xe and NaI) did not yet reach a level which allows us to obtain new decisive constraints on the SUSY parameters. Future about two-orders-of-magnitude improvement of the background index in the HDMS experiment [19] can in principle supply us with new constraints for the SUSY models. We also noticed that the DAMA evidence favors the light Higgs sector in the effMSSM (which could be reached at LHC), a high event rate in a ^{73}Ge detector and relatively high upgoing muon fluxes from relic neutralino annihilations in the Earth and the Sun.

The performed calculations allow direct comparison of sensitivities of different dark matter setups to the WIMPs expected from the measurements of the DAMA experiment. In particular, it is shown that detectors with a ^{73}Ge , ^{129}Xe , and NaI target have better prospects to confirm or to reject the DAMA result.

Now those spin structure functions are available for almost all experimentally interesting nuclei, they could be coherently used by all experimental groups. This will make easier and more reliable comparisons between results of different dark matter search experiments and put it on the equal footing [60]. It will also allow one to reduce significantly the nuclear physics systematic uncertainties in the analysis of the data.

This work was supported in part by JINR–Slovak Republic programme and the Russian Foundation for Basic Research (grant 06-02-04003). Author thanks Dr. F. Simkovic and Prof. H. V. Klapdor-Kleingrothaus for permanent and very fruitful collaboration and Dr. V. A. Kuzmin (JINR) for useful discussions.

Appendix

A. ELEMENTS OF NUCLEAR STRUCTURE CALCULATIONS

For completeness we collect in this appendix some formulas which allow one to connect the WIMP–nucleon scattering with the WIMP–nuclear scattering. We follow directly Engel et al. [21, 56]. The low-energy effective WIMP–nucleon Lagrangian is $\mathcal{L}_{\text{eff}} = \bar{\chi}\gamma^\mu\gamma_5\chi \cdot \mathcal{J}_\mu(x)$, where $\mathcal{J}_\mu(x) \propto N\gamma_\mu\gamma_5N$ is the nucleon

current. The one-nucleon matrix element of the current at finite q takes the approximate form

$$\begin{aligned} \langle p, s | \mathcal{J}_\mu(x) | p', s' \rangle &= \\ &= \bar{U}_N(p, s) \left(\frac{a_0 + a_1 \tau_3}{2} \gamma_\mu \gamma_5 + \frac{m_N a_1 \tau_3}{q^2 + m_\pi^2} q_\mu \gamma_5 \right) U_N(p', s') e^{iq^\nu x_\mu}. \end{aligned} \quad (33)$$

Here $q_\mu = p_\mu - p'_\mu$, $U_N(p, s)$ is the nucleon 4-component spinor and the energy transfer q_0 was assumed to be very small. In the nonrelativistic limit the time component of current (33) is proportional to $v/c \approx 10^{-3}$ and can be safely neglected. For the spatial component of the current one has the following expression:

$$\langle p, s | \mathcal{J}_\mu(x) | p', s' \rangle = \left\langle s \left| \frac{a_0 + a_1 \tau_3}{2} \boldsymbol{\sigma} - \frac{(\boldsymbol{\sigma} \cdot \mathbf{q}) a_1 \tau_3}{2(q^2 + m_\pi^2)} \mathbf{q} \right| s' \right\rangle e^{iq^\nu x_\mu}, \quad (34)$$

where $|s\rangle$ and $|s'\rangle$ are two-component spinors. To obtain the cross section for scattering of the WIMP from nuclei one must evaluate the matrix element of the nucleon current between many-nucleon states. In the impulse approximation the cross section is

$$\frac{d\sigma^A}{dq^2}(v, q^2) = \frac{|\mathcal{M}|^2}{v^2(2J+1)\pi}, \quad (35)$$

$$\mathcal{M} = \langle s | \boldsymbol{\sigma}_\chi | s' \rangle \int d^3x \langle J, M | \mathcal{J}(\mathbf{x}) | J, M' \rangle e^{i\mathbf{q} \cdot \mathbf{x}},$$

where $|\mathcal{M}|^2$ is summed over s, s', M, M' . Here J is the angular momentum of the ground state and the nuclear current $\mathcal{J}(\mathbf{x})$ is given by the sum over all nucleons with current matrix elements from (34). Expanding the current in vector spherical harmonics one obtains the form given in (2) and (6):

$$\begin{aligned} \frac{d\sigma_{\text{SD}}^A}{dq^2}(v, q^2) &= \frac{S_{\text{SD}}^A(q^2)}{v^2(2J+1)}, \\ S_{\text{SD}}^A(q) &= \sum_{L \text{ odd}} (|\langle N | \mathcal{T}_L^{\text{el5}}(q) | N \rangle|^2 + |\langle N | \mathcal{L}_L^5(q) | N \rangle|^2). \end{aligned}$$

The transverse electric $\mathcal{T}^{\text{el5}}(q)$ and longitudinal $\mathcal{L}^5(q)$ multipole projections of the axial vector current operator as well as the scalar function $\mathcal{C}_L(q)$ are given

by [21, 56, 57]:

$$\begin{aligned}
 \mathcal{T}_L^{\text{el5}}(q) &= \frac{1}{\sqrt{2L+1}} \sum_i \frac{a_0 + a_1 \tau_3^i}{2} \left[-\sqrt{L} M_{L,L+1}(q\mathbf{r}_i) + \sqrt{L+1} M_{L,L-1}(q\mathbf{r}_i) \right], \\
 \mathcal{L}_L^5(q) &= \frac{1}{\sqrt{2L+1}} \sum_i \left(\frac{a_0}{2} + \frac{a_1 m_\pi^2 \tau_3^i}{2(q^2 + m_\pi^2)} \right) \times \\
 &\quad \times \left[\sqrt{L+1} M_{L,L+1}(q\mathbf{r}_i) + \sqrt{L} M_{L,L-1}(q\mathbf{r}_i) \right], \\
 \mathcal{C}_L(q) &= \sum_{i, \text{ nucleons}} C_0^E j_L(qr_i) Y_L(\hat{r}_i), \quad C_0(q) = \sum_i C_0^E j_0(qr_i) Y_0(\hat{r}_i), \quad (36)
 \end{aligned}$$

where $M_{L,L'}(q\mathbf{r}_i) = j_{L'}(qr_i) [Y_{L'}(\hat{r}_i) \boldsymbol{\sigma}_i]^L$, m_π is the pion mass and $a_{0(1)}$ is the isoscalar (isovector) effective spin-dependent WIMP–nucleon coupling. In the limit of zero-momentum transfer $S_{\text{SD}}^A(q)$ reduces to

$$\begin{aligned}
 S_{\text{SD}}^A(0) &= \frac{1}{4\pi} \left| \langle N | \sum_i \frac{1}{2} (a_0 + a_1 \tau_3^i) \boldsymbol{\sigma}_i | N \rangle \right|^2 = \\
 &= \frac{1}{4\pi} |(a_0 + a_1) \langle N | \mathbf{S}_p | N \rangle + (a_0 - a_1) \langle N | \mathbf{S}_n | N \rangle|^2 = \quad (37) \\
 &= \frac{1}{\pi} \frac{(2J+1)(J+1)}{J} |a_p \langle N | \mathbf{S}_p | N \rangle + a_n \langle N | \mathbf{S}_n | N \rangle|^2 = \\
 &= \frac{2J+1}{\pi} J(J+1) \Lambda^2, \quad (38)
 \end{aligned}$$

with $\Lambda = \frac{\langle N | a_p \mathbf{S}_p + a_n \mathbf{S}_n | N \rangle}{J} = \frac{a_p \langle \mathbf{S}_p \rangle}{J} + \frac{a_n \langle \mathbf{S}_n \rangle}{J}$.

In accordance with convention, the Z components of the angular momentum and spin operators are evaluated in the maximal M_J state, e.g., $\langle \mathbf{S} \rangle \equiv \langle N | \mathbf{S} | N \rangle = \langle J, M_J = J | S_z | J, M_J = J \rangle$.

In the ISPSM only the last odd nucleon contributes to the spin and the angular momentum of the nucleus. In this limit

$$\langle \mathbf{S}_n^A \rangle = \frac{J_A(J_A + 1) - L_A(L_A + 1) + 3/4}{2J_A + 2}, \quad (39)$$

where J_A and L_A are the single-particle total and angular momenta. They are deduced from the measured nuclear angular momentum and the parity.

B. NUCLEON SPIN STRUCTURE

To evaluate the spin content of the nucleon one needs the matrix element of the effective quark axial-vector current $J^\mu = \bar{q} \gamma^\mu \gamma_5 q$ in the nucleon [46]. These

matrix elements

$$\langle (p, n) | \bar{q} \gamma_\mu \gamma_5 q | (p, n) \rangle = 2s_\mu^{(p,n)} \Delta q^{(p,n)} \quad (40)$$

are proportional to the spin of the neutron (proton or neutron), $s_\mu^{(p,n)}$. The quantities $\Delta q^{(p,n)}$ are usually extracted from the data obtained in polarized lepton–nucleon deep inelastic scattering. Uncertainties in the experimentally determined values for the quantities Δq can lead to significant variations in the WIMP–nucleon axial-vector coupling, and therefore to the predicted rates for detection of WIMPs which have primarily spin couplings to nuclei [46]. With definition (40) the effective spin-dependent interaction of neutralinos with the nucleon has the form

$$\mathcal{L}_{\text{spin}} = 2\bar{\chi} \gamma^\mu \gamma_5 \chi \bar{n} s_\mu n \sum_{q=u,d,s} \mathcal{A}_q \Delta q^{(n)}. \quad (41)$$

Recent global QCD analysis for the g_1 structure functions [159], including $\mathcal{O}(\alpha_s^3)$ corrections, corresponds to the following values of spin nucleon parameters [137]:

$$\begin{aligned} \Delta_u^{(p)} = \Delta_d^{(n)} &= 0.78 \pm 0.02, & \Delta_d^{(p)} = \Delta_u^{(n)} &= -0.48 \pm 0.02, \\ \Delta_s^{(p)} = \Delta_s^{(n)} &= -0.15 \pm 0.02. \end{aligned}$$

It is also more accurate

$$c_0^{p,n} = \sum_{q=u,d,s} f_{Tq}^{(p,n)} \mathcal{C}_q + \frac{2}{27} f_{TG}^{(p,n)} \sum_{c,b,t} \mathcal{C}_q.$$

The parameters $f_{Tq}^{(p,n)}$ and $f_{TG}^{(p,n)}$ are defined by

$$m_p f_{Tq}^{(p)} \equiv \langle p | m_q \bar{q} q | p \rangle, \quad f_{TG}^{(p,n)} = 1 - \sum_{q=u,d,s} f_{Tq}^{(p,n)}.$$

Following [137] we use the updated parameters:

$$f_{Tu}^{(p)} = 0.020 \pm 0.004, \quad f_{Td}^{(p)} = 0.026 \pm 0.005, \quad f_{Ts}^{(p)} = 0.118 \pm 0.062; \quad (42)$$

$$f_{Tu}^{(n)} = 0.014 \pm 0.003, \quad f_{Td}^{(n)} = 0.036 \pm 0.008, \quad f_{Ts}^{(n)} = 0.118 \pm 0.062. \quad (43)$$

Our estimations of the effect of the inaccuracy in the determination of f_{Ts} on the total event rate agree with those obtained before in [49] and in [97, 99, 112]. The inaccuracy maximally changes the proton–neutralino cross section (event rate) within about one order of magnitude. The value chosen in this work gives probably a more pessimistic view of the cross sections. The inaccuracy of other parameters has a smaller effect on the cross sections.

C. EFFECTIVE NEUTRALINO–QUARK LAGRANGIAN

The axial-vector and scalar interaction of a neutralino with a quark q is given by

$$\mathcal{L}_{\text{eff}} = \mathcal{A}_q \bar{\chi} \gamma_\mu \gamma_5 \chi \bar{q} \gamma^\mu \gamma_5 q + \mathcal{C}_q \bar{\chi} \chi \bar{q} q O(1/m_{\tilde{q}}^4).$$

The terms with vector and pseudoscalar quark currents are omitted being negligible in the case of nonrelativistic DM neutralinos with typical velocities $v_\chi \approx 10^{-3}c$. The Feynman diagrams which give rise to the effective neutralino–quark axial-vector couplings

$$\begin{aligned} \mathcal{A}_q = & -\frac{g^2}{4M_W^2} \left[\frac{\mathcal{N}_{14}^2 - \mathcal{N}_{13}^2}{2} T_3 - \frac{M_W^2}{m_{\tilde{q}1}^2 - (m_\chi + m_q)^2} \times \right. \\ & \times (\cos^2 \theta_q \phi_{qL}^2 + \sin^2 \theta_q \phi_{qR}^2) - \frac{M_W^2}{m_{\tilde{q}2}^2 - (m_\chi + m_q)^2} (\sin^2 \theta_q \phi_{qL}^2 + \cos^2 \theta_q \phi_{qR}^2) - \\ & - \frac{m_q^2}{4} P_q^2 \left(\frac{1}{m_{\tilde{q}1}^2 - (m_\chi + m_q)^2} + \frac{1}{m_{\tilde{q}2}^2 - (m_\chi + m_q)^2} \right) - \\ & - \frac{m_q}{2} M_W P_q \sin 2\theta_q T_3 (\mathcal{N}_{12} - \tan \theta_W \mathcal{N}_{11}) \times \\ & \left. \times \left(\frac{1}{m_{\tilde{q}1}^2 - (m_\chi + m_q)^2} - \frac{1}{m_{\tilde{q}2}^2 - (m_\chi + m_q)^2} \right) \right] \end{aligned}$$

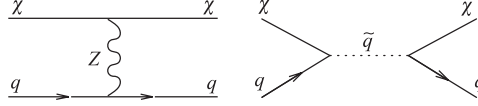


Fig. 28. Spin-dependent elastic scattering of neutralinos from quarks

are shown in Fig.28. The first term in \mathcal{A}_q comes from Z^0 exchange, and the other terms come from squark exchanges. The Feynman diagrams which give rise to the effective neutralino–quark scalar couplings

$$\begin{aligned} \mathcal{C}_q = & -\frac{m_q}{M_W} \frac{g^2}{4} \left[\frac{F_h}{m_h^2} h_q + \frac{F_H}{m_H^2} H_q + \left(\frac{m_q}{4M_W} P_q^2 - \frac{M_W}{m_q} \phi_{qL} \phi_{qR} \right) \times \right. \\ & \times \left(\frac{\sin 2\theta_q}{m_{\tilde{q}1}^2 - (m_\chi + m_q)^2} - \frac{\sin 2\theta_q}{m_{\tilde{q}2}^2 - (m_\chi + m_q)^2} \right) + \\ & \left. + P_q \left(\frac{\cos^2 \theta_q \phi_{qL} - \sin^2 \theta_q \phi_{qR}}{m_{\tilde{q}1}^2 - (m_\chi + m_q)^2} - \frac{\cos^2 \theta_q \phi_{qR} - \sin^2 \theta_q \phi_{qL}}{m_{\tilde{q}2}^2 - (m_\chi + m_q)^2} \right) \right], \end{aligned}$$

where

$$\begin{aligned}
 F_h &= (\mathcal{N}_{12} - \mathcal{N}_{11} \tan \theta_W)(\mathcal{N}_{14} \cos \alpha_H + \mathcal{N}_{13} \sin \alpha_H), \\
 F_H &= (\mathcal{N}_{12} - \mathcal{N}_{11} \tan \theta_W)(\mathcal{N}_{14} \sin \alpha_H - \mathcal{N}_{13} \cos \alpha_H), \\
 h_q &= \left(\frac{1}{2} + T_3\right) \frac{\cos \alpha_H}{\sin \beta} - \left(\frac{1}{2} - T_3\right) \frac{\sin \alpha_H}{\cos \beta}, \\
 H_q &= \left(\frac{1}{2} + T_3\right) \frac{\sin \alpha_H}{\sin \beta} + \left(\frac{1}{2} - T_3\right) \frac{\cos \alpha_H}{\cos \beta}, \\
 \phi_{qL} &= \mathcal{N}_{12} T_3 + \mathcal{N}_{11}(Q - T_3) \tan \theta_W, \quad \phi_{qR} = \tan \theta_W Q \mathcal{N}_{11}, \\
 P_q &= \left(\frac{1}{2} + T_3\right) \frac{\mathcal{N}_{14}}{\sin \beta} + \left(\frac{1}{2} - T_3\right) \frac{\mathcal{N}_{13}}{\cos \beta},
 \end{aligned}$$

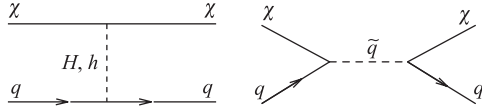


Fig. 29. Spin-independent or scalar (tree level) elastic scattering of neutralinos from quarks

are shown in Fig. 29. The importance of these scalar spin-independent contribution was found by K. Griest in [160].

D. SUSY PARTICLE SPECTRUM

For completeness, we collect here formulas for masses of the SUSY particles in the MSSM. There are four Higgs bosons — neutral CP -odd (A), CP -even (H, h), charged (H^\pm). The CP -even Higgs boson mass matrix has the form:

$$\begin{aligned}
 \begin{pmatrix} H_{11} & H_{12} \\ H_{12} & H_{22} \end{pmatrix} &= \frac{1}{2} \begin{pmatrix} \tan \beta & -1 \\ -1 & \cot \beta \end{pmatrix} M_A^2 \sin 2\beta + \\
 &+ \frac{1}{2} \begin{pmatrix} \cot \beta & -1 \\ -1 & \tan \beta \end{pmatrix} m_Z^2 \sin 2\beta + \omega \begin{pmatrix} \Delta_{11} & \Delta_{12} \\ \Delta_{12} & \Delta_{22} \end{pmatrix},
 \end{aligned}$$

$$H_{11} = \frac{\sin 2\beta}{2} \left(\frac{m_Z^2}{\tan \beta} + M_A^2 \tan \beta \right) + \omega \Delta_{11},$$

$$H_{22} = \frac{\sin 2\beta}{2} \left(m_Z^2 \tan \beta + \frac{M_A^2}{\tan \beta} \right) + \omega \Delta_{22},$$

$$H_{12} = H_{21} = -\frac{\sin 2\beta}{2} (m_Z^2 + M_A^2) + \omega \Delta_{12}.$$

For example, Δ_{11} which includes loop corrections is

$$\begin{aligned} \Delta_{11} = & \frac{m_b^4}{c_\beta^2} \left(\ln \frac{m_{b_1}^2 m_{b_2}^2}{m_b^4} + \frac{2A_b(A_b - \mu \tan \beta)}{m_{b_1}^2 - m_{b_2}^2} \ln \frac{m_{b_1}^2}{m_{b_2}^2} \right) + \\ & + \frac{m_b^4}{c_\beta^2} \left(\frac{A_b(A_b - \mu \tan \beta)}{m_{b_1}^2 - m_{b_2}^2} \right)^2 g(m_{b_1}^2, m_{b_2}^2) + \\ & + \frac{m_t^4}{s_\beta^2} \left(\frac{\mu \left(A_t - \frac{\mu}{\tan \beta} \right)}{m_{t_1}^2 - m_{t_2}^2} \right)^2 g(m_{t_1}^2, m_{t_2}^2). \end{aligned}$$

$$\omega = \frac{3g_2^2}{16\pi^2 m_W^2} c_\beta^2 = \cos^2 \beta, \quad s_\beta^2 = \sin^2 \beta, \quad g(m_1^2, m_2^2) = 2 - \frac{m_1^2 + m_2^2}{m_1^2 - m_2^2} \ln \frac{m_1^2}{m_2^2}.$$

The diagonalization of the above matrix gives the Higgs boson masses $m_{H,h}$.

$$\begin{aligned} m_{H,h}^2 &= \frac{1}{2} \left\{ H_{11} + H_{22} \pm \sqrt{(H_{11} + H_{22})^2 - 4(H_{11}H_{22} - H_{12}^2)} \right\}, \\ m_{H^\pm}^2 &= m_W^2 + M_A^2 + \omega \Delta_{\text{ch}}. \end{aligned}$$

Here m_{H^\pm} is the charged Higgs boson mass in the one-loop approximation. The mixing angle α_H is obtained from

$$\sin 2\alpha_H = \frac{2H_{12}^2}{m_{H_1^0}^2 - m_{H_2^0}^2}, \quad \cos 2\alpha_H = \frac{H_{11}^2 - H_{22}^2}{m_{H_1^0}^2 - m_{H_2^0}^2}.$$

The neutralino mass matrix in the basis $(\tilde{B}, \tilde{W}^3, \tilde{H}_1^0, \tilde{H}_2^0)$ has the form:

$$\begin{aligned} \mathcal{M}_\chi &= \\ &= \begin{pmatrix} M_1 & 0 & -M_Z \cos \beta \sin \theta_W & M_Z \sin \beta \sin \theta_W \\ 0 & M_2 & M_Z \cos \beta \cos \theta_W & -M_Z \sin \beta \cos \theta_W \\ -M_Z \cos \beta \sin \theta_W & M_Z \cos \beta \cos \theta_W & 0 & -\mu \\ M_Z \sin \beta \sin \theta_W & -M_Z \sin \beta \cos \theta_W & -\mu & 0 \end{pmatrix}. \end{aligned}$$

The diagonalization gives mass eigenstates (4 neutralinos):

$$\chi_i(m_{\chi_i}) = \mathcal{N}_{i1} \tilde{B} + \mathcal{N}_{i2} \tilde{W}^3 + \mathcal{N}_{i3} \tilde{H}_1^0 + \mathcal{N}_{i4} \tilde{H}_2^0.$$

The lightest (LSP) $\chi = \chi_1$ is the best DM candidate. The chargino mass term is

$$\left(\tilde{W}^-, \tilde{H}_1^- \right) \begin{pmatrix} M_2 & \sqrt{2} M_W \sin \beta \\ \sqrt{2} M_W \cos \beta & \mu \end{pmatrix} \begin{pmatrix} \tilde{W}^+ \\ \tilde{H}_2^+ \end{pmatrix} + \text{h.c.}$$

The diagonalization $U^* \mathcal{M}_{\tilde{\chi}^\pm} V^\dagger = \text{diag}(M_{\tilde{\chi}_1^\pm}, M_{\tilde{\chi}_2^\pm})$ gives charged mass eigenstates

$$\tilde{\chi}^- = U_{i1} \tilde{W}^- + U_{i2} \tilde{H}^-, \quad \tilde{\chi}^+ = V_{i1} \tilde{W}^+ + V_{i2} \tilde{H}^+$$

with masses

$$M_{\tilde{\chi}_{1,2}^\pm}^2 = \frac{1}{2} \left[M_2^2 + \mu^2 + 2M_W^2 \mp \sqrt{(M_2^2 - \mu^2)^2 + 4M_W^4 \cos^2 2\beta + 4M_W^2 (M_2^2 + \mu^2 + 2M_2 \mu \sin 2\beta)} \right].$$

The sfermion mass matrices \mathcal{M}_t^2 , \mathcal{M}_b^2 , and \mathcal{M}_τ^2 have the form:

$$\mathcal{M}_t^2 = \begin{bmatrix} m_Q^2 + m_t^2 + \frac{1}{6}(4M_W^2 - M_Z^2) \cos 2\beta & m_t(A_t - \mu \cot \beta) \\ m_t(A_t - \mu \cot \beta) & m_U^2 + m_t^2 - \frac{2}{3}(M_W^2 - M_Z^2) \cos 2\beta \end{bmatrix},$$

$$\mathcal{M}_b^2 = \begin{bmatrix} m_Q^2 + m_b^2 - \frac{1}{6}(2M_W^2 + M_Z^2) \cos 2\beta & m_b(A_b - \mu \tan \beta) \\ m_b(A_b - \mu \tan \beta) & m_D^2 + m_b^2 + \frac{1}{3}(M_W^2 - M_Z^2) \cos 2\beta \end{bmatrix},$$

$$\mathcal{M}_\tau^2 = \begin{bmatrix} m_L^2 + m_\tau^2 - \frac{1}{2}(2M_W^2 - M_Z^2) \cos 2\beta & m_\tau(A_\tau - \mu \tan \beta) \\ m_\tau(A_\tau - \mu \tan \beta) & m_E^2 + m_\tau^2 + (M_W^2 - M_Z^2) \cos 2\beta \end{bmatrix}.$$

It is worth noting that these masses as well as the above-mentioned couplings of neutralino–quark interactions \mathcal{A}_q and \mathcal{C}_q are functions of the common set of SUSY parameters like, for example, $\tan \beta$, M_A , μ , A_q , etc. The set of parameters allows one to describe observables at the highest and lowest energies coherently and simultaneously.

REFERENCES

1. *Spergel D. N. et al.* // *Astrophys. J. Suppl.* 2003. V. 148. P. 175; astro-ph/0302209.
2. *Bennett C. L. et al.* // *Astrophys. J. Suppl.* 2003. V. 148. P. 1; astro-ph/0302207.
3. *Bergstrom L.* // *Rep. Prog. Phys.* 2000. V. 63. P. 793; hep-ph/0002126.
4. *de Bernardis P. et al.* // *Nature.* 2000. V. 404. P. 955–959; astro-ph/0004404.
5. *Balbi A. et al.* // *Astrophys. J.* 2000. V. 545. P. L1–L4; astro-ph/0005124.
6. *Bernabei R. et al.* // *Phys. Lett. B.* 2000. V. 480. P. 23–31.
7. *Bernabei R. et al.* // *Riv. Nuovo Cim.* 2003. V. 26. P. 1–73; astro-ph/0307403.
8. *Bernabei R. et al.* astro-ph/0311046.
9. *Bednyakov V. A., Klapdor-Kleingrothaus H. V.* // *Phys. Rev. D.* 2001. V. 63. P. 095005; hep-ph/0011233.

10. *Ellis J. R. et al.* hep-ph/0308075.
11. *Ellis J. R. et al.* Phys. Rev. D. 2003. V. 67. P. 123502; hep-ph/0302032.
12. *Copi C. J., Krauss L. M.* // Phys. Rev. D. 2003. V. 67. P. 103507; astro-ph/0208010.
13. *Kurylov A., Kamionkowski M.* // Phys. Rev. D. 2004. V. 69. P. 063503; hep-ph/0307185.
14. *Tucker-Smith D., Weiner N.* // Phys. Rev. D. 2005. V. 72. P. 063509; hep-ph/0402065.
15. *Gelmini G., Gondolo P.* hep-ph/0405278.
16. *Bottino A. et al.* // Phys. Rev. D. 2005. V. 72. P. 083521; hep-ph/0508270.
17. *Klapdor-Kleingrothaus H. V. et al.* // Nucl. Instr. Meth. A. 2003. V. 511. P. 341–346; hep-ph/0309170.
18. *Tomei C. et al.* // Nucl. Instr. Meth. A. 2003. V. 508. P. 343–352; hep-ph/0306257.
19. *Klapdor-Kleingrothaus H. V. et al.* // Astropart. Phys. 2003. V. 18. P. 525–530; hep-ph/0206151.
20. *Bednyakov V. A., Simkovic F.* // Phys. Rev. D. 2005. V. 72. P. 035015; hep-ph/0506195.
21. *Engel J.* // Phys. Lett. B. 1991. V. 264. P. 114–119.
22. *Bottino A. et al.* hep-ph/0307303.
23. *Bednyakov V. A., Klapdor-Kleingrothaus H. V., Kovalenko S. G.* // Phys. Lett. B. 1994. V. 329. P. 5–9; hep-ph/9401271.
24. *Bednyakov V. A.* // Phys. At. Nucl. 2003. V. 66. P. 490–493; hep-ph/0201046.
25. *Bednyakov V. A.* // Phys. At. Nucl. 2004. V. 67. P. 1931–1941; hep-ph/0310041.
26. *Bednyakov V. A., Simkovic F.* // Part. Nucl. 2005. V. 36. P. 131–152; hep-ph/0406218.
27. *Bednyakov V. A., Klapdor-Kleingrothaus H. V.* hep-ph/0504031.
28. *Girard T. A. et al.* // Phys. Lett. B. 2005. V. 621. P. 233–238; hep-ex/0505053.
29. *Girard T. A. et al.* hep-ex/0504022.
30. *Giuliani F.* // Phys. Rev. Lett. 2004. V. 93. P. 161301; hep-ph/0404010.
31. *Giuliani F., Girard T. A.* // Phys. Rev. D. 2005. V. 71. P. 123503; hep-ph/0502232.
32. *Savage C., Gondolo P., Freese K.* // Phys. Rev. D. 2004. V. 70. P. 123513; astro-ph/0408346.
33. *Benoit A. et al.* // Phys. Lett. B. 2005. V. 616. P. 25–30; astro-ph/0412061.
34. *Tanimori T. et al.* // Phys. Lett. B. 2004. V. 578. P. 241–246; astro-ph/0310638.
35. *Ovchinnikov B. M., Parusov V. V.* The Preparing of an Experiment for Search for Spin-Dependent Interactions of WIMP. INR Preprint 1097/2003. 2003.
36. *Moulin E., Mayet F., Santos D.* // Phys. Lett. B. 2005. V. 614. P. 143–154; astro-ph/0503436.
37. *Mayet F. et al.* // Phys. Lett. B. 2002. V. 538. P. 257; astro-ph/0201097.
38. *Klapdor-Kleingrothaus H. V., Krivosheina I. V., Tomei C.* // Phys. Lett. B. 2005. V. 609. P. 226–231.
39. *Ahner G. J. et al.* // Nucl. Instr. Meth. A. 2004. V. 535. P. 644–655.
40. *Snowden-Ifft D. P., Martoff C. J., Burwell J. M.* // Phys. Rev. D. 2000. V. 61. P. 101301; astro-ph/9904064.
41. *Gaitskell R. J. et al.* // Nucl. Instr. Meth. A. 1996. V. 370. P. 162–164.
42. *Sekiya H. et al.* astro-ph/0405598.
43. *Morgan B., Green A. M., Spooner N. J. C.* // Phys. Rev. D. 2005. V. 71. P. 103507; astro-ph/0408047.

44. Vergados J. D. // Part. Nucl., Lett. 2001. No. 3[106]. P. 74–108; hep-ph/0010151.
45. Vergados J. D. // Phys. At. Nucl. 2003. V. 66. P. 481–489; hep-ph/0201014.
46. Jungman G., Kamionkowski M., Griest K. // Phys. Rep. 1996. V. 267. P. 195–373; hep-ph/9506380.
47. Divari P. C. et al. // Phys. Rev. C. 2000. V. 61. P. 054612.
48. Bednyakov V. A., Klapdor-Kleingrothaus H. V., Kovalenko S. G. // Phys. Rev. D. 1997. V. 55. P. 503–514; hep-ph/9608241.
49. Bednyakov V. A., Klapdor-Kleingrothaus H. V., Kovalenko S. // Phys. Rev. D. 1994. V. 50. P. 7128–7143; hep-ph/9401262.
50. Bednyakov V. A., Klapdor-Kleingrothaus H. V. // Phys. Rev. D. 2000. V. 62. P. 043524; hep-ph/9908427.
51. Lewin J. D., Smith P. F. // Astropart. Phys. 1996. V. 6. P. 87–112.
52. Smith P. F., Lewin J. D. // Phys. Rep. 1990. V. 187. P. 203.
53. Bednyakov V. A., Klapdor-Kleingrothaus H. V. // Phys. At. Nucl. 1999. V. 62. P. 966–974.
54. Bednyakov V. A., Kovalenko S. G., Klapdor-Kleingrothaus H. V. // Phys. At. Nucl. 1996. V. 59. P. 1718–1727.
55. Bednyakov V. A. et al. // Z. Phys. A. 1997. Bd. 357. S. 339–347; hep-ph/9606261.
56. Engel J., Pittel S., Vogel P. // Intern. J. Mod. Phys. E. 1992. V. 1. P. 1–37.
57. Ressel M. T. et al. // Phys. Rev. D. 1993. V. 48. P. 5519–5535.
58. Bernabei R. et al. // Phys. Lett. B. 2001. V. 509. P. 197–203.
59. Engel J. et al. // Phys. Rev. C. 1995. V. 52. P. 2216–2221; hep-ph/9504322.
60. Ressel M. T., Dean D. J. // Phys. Rev. C. 1997. V. 56. P. 535–546; hep-ph/9702290.
61. Griest K. // Phys. Rev. D. 1988. V. 38. P. 2357.
62. Ellis J. R., Flores R. A. // Nucl. Phys. B. 1988. V. 307. P. 883.
63. Ellis J. R., Flores R. A. // Phys. Lett. B. 1991. V. 263. P. 259–266.
64. Engel J., Vogel P. // Phys. Rev. D. 1989. V. 40. P. 3132–3135.
65. Pacheco A. F., Strottman D. // Ibid. P. 2131–2133.
66. Iachello F., Krauss L. M., Maino G. // Phys. Lett. B. 1991. V. 254. P. 220–224.
67. Nikolaev M. A., Klapdor-Kleingrothaus H. V. // Z. Phys. A. 1993. Bd. 345. S. 373–376.
68. Dimitrov V., Engel J., Pittel S. // Phys. Rev. D. 1995. V. 51. P. 291–295; hep-ph/9408246.
69. Ellis J. R., Flores R. A. // Nucl. Phys. B. 1993. V. 400. P. 25–36.
70. Bednyakov V. A., Klapdor-Kleingrothaus H. V. // Phys. Rev. D. 2004. V. 70. P. 096006; hep-ph/0404102.
71. Bernabei R. et al. astro-ph/0305542.
72. Bednyakov V. A., Simkovic F. // Part. Nucl. 2006. V. 37, No. 7.
73. Vergados J. D. // J. Phys. 1996. G. V. 22. P. 253–272; hep-ph/9504320.
74. Engel J. et al. // Phys. Lett. B. 1992. V. 275. P. 119–123.
75. Nikolaev M. A., Klapdor-Kleingrothaus H. V. // Z. Phys. A. 1993. Bd. 345. S. 183–186.
76. Kosmas T. S., Vergados J. D. // Phys. Rev. D. 1997. V. 55. P. 1752–1764; hep-ph/9701205.
77. Goodman M. W., Witten E. // Phys. Rev. D. 1985. V. 31. P. 3059.

78. *Drukier A. K., Freese K., Spergel D. N.* // Phys. Rev. D. 1986. V. 33. P. 3495–3508.
79. *Tovey D. R. et al.* // Phys. Lett. B. 2000. V. 488. P. 17–26; hep-ph/0005041.
80. *Mandic V. et al.* hep-ph/0008022.
81. *Bergstrom L., Gondolo P.* // Astropart. Phys. 1996. V. 5. P. 263–278; hep-ph/9510252.
82. *Gondolo P.* hep-ph/0005171.
83. *Bednyakov V. A., Klapdor-Kleingrothaus H. V., Gronewold V.* // Phys. Rev. D. 2002. V. 66. P. 115005; hep-ph/0208178.
84. *Bednyakov V. A., Klapdor-Kleingrothaus H. V., Zaiti E.* // Phys. Rev. D. 2002. V. 66. P. 015010; hep-ph/0203108.
85. *Bednyakov V. A.* hep-ph/0208172.
86. *Bottino A. et al.* // Phys. Rev. D. 2001. V. 63. P. 125003; hep-ph/0010203.
87. *Hagiwara K. et al.* // Phys. Rev. D. 2002. V. 66. P. 010001.
88. *Alam M. S. et al.* // Phys. Rev. Lett. 1995. V. 74. P. 2885–2889.
89. *Abe K. et al.* hep-ex/0107065.
90. *Bertolini S. et al.* // Nucl. Phys. B. 1991. V. 353. P. 591–649.
91. *Barbieri R., Giudice G. F.* // Phys. Lett. B. 1993. V. 309. P. 86–90; hep-ph/9303270.
92. *Buras A. J. et al.* // Nucl. Phys. B. 1994. V. 424. P. 374–398; hep-ph/9311345.
93. *Ali A., Greub C.* // Z. Phys. C. 1993. Bd. 60. S. 433–442.
94. *Gondolo P. et al.* astro-ph/0012234.
95. *Bednyakov V. A., Klapdor-Kleingrothaus H. V., Tu H.* // Phys. Rev. D. 2001. V. 64. P. 075004; hep-ph/0101223.
96. *Drees M. et al.* // Phys. Rev. D. 2001. V. 63. P. 035008; hep-ph/0007202.
97. *Arnowitz R., Dutta B., Santoso Y.* hep-ph/0008336.
98. *Corsetti A., Nath P.* hep-ph/0005234.
99. *Feng J. L., Matchev K. T., Wilczek F.* // Phys. Lett. B. 2000. V. 482. P. 388–399; hep-ph/0004043.
100. *Accomando E. et al.* // Nucl. Phys. B. 2000. V. 585. P. 124–142; hep-ph/0001019.
101. *Gabrielli E. et al.* // Phys. Rev. D. 2001. V. 63. P. 025008; hep-ph/0006266.
102. *Baer H., Brhlik M.* // Phys. Rev. D. 1998. V. 57. P. 567–577; hep-ph/9706509.
103. *Lahanas A. B., Nanopoulos D. V., Spanos V. C.* // Mod. Phys. Lett. A. 2001. V. 16. P. 1229–1242; hep-ph/0009065.
104. *Ullio P., Kamionkowski M., Vogel P.* // JHEP. 2001. 07. 044; hep-ph/0010036.
105. *Drees M., Nojiri M.* // Phys. Rev. D. 1993. V. 48. P. 3483–3501; hep-ph/9307208.
106. *Bottino A. et al.* // Phys. Lett. B. 1997. V. 402. P. 113–121; hep-ph/9612451.
107. *Klapdor-Kleingrothaus H. V.* // Nucl. Phys. Proc. Suppl. 2002. V. 110. P. 364–368; hep-ph/0206249.
108. *Klapdor-Kleingrothaus H. V. et al.* hep-ph/9910205.
109. *Hellmig J., Klapdor-Kleingrothaus H. V.* // Z. Phys. A. 1997. Bd. 359. S. 351–359; nucl-ex/9801004.
110. *Klapdor-Kleingrothaus H. V., Hirsch M.* // Z. Phys. A. 1997. Bd. 359. S. 361–372.

111. *Bednyakov V.A., Klapdor-Kleingrothaus H.V.* // Phys. Rev. D. 1999. V.59. P.023514; hep-ph/9802344.
112. *Ellis J.R., Ferstl A., Olive K.A.* // Phys. Rev. D. 2001. V.63. P.065016; hep-ph/0007113.
113. *Bacci C. et al.* // Nucl. Phys. Proc. Suppl. 1994. V.35. P.159–161.
114. *Bacci C. et al.* // Phys. Lett. B. 1992. V.293. P.460–464.
115. *Bacci C. et al.* // Astropart. Phys. 1994. V.2. P.117–126.
116. *de Bellefon A. et al.* // Astropart. Phys. 1996. V.6. P.35–44.
117. *Bernabei R. et al.* // Phys. Lett. B. 1996. V.389. P.757–766.
118. *Bernabei R. et al.* // Astropart. Phys. 1997. V.7. P.73–76.
119. *Belli P. et al.* // Nucl. Phys. B. 1999. V.563. P.97–106.
120. *Sarsa M.L. et al.* // Phys. Lett. B. 1996. V.386. P.458–462.
121. *Smith P.F. et al.* // Ibid. V.379. P.299–308.
122. *Sumner T.J. et al.* // Nucl. Phys. Proc. Suppl. 1999. V.70. P.74–78.
123. *Spooner N.J.C. et al.* // Phys. Lett. B. 2000. V.473. P.330–336.
124. *Ogawa I. et al.* // Nucl. Phys. A. 2000. V.663. P.869–872.
125. *Fushimi K. et al.* // Astropart. Phys. 1999. V.12. P.185–192.
126. *Yoshida S. et al.* // Nucl. Phys. Proc. Suppl. 2000. V.87. P.58–60.
127. *Ootani W. et al.* // Astropart. Phys. 1998. V.9. P.325–329.
128. *Minowa M.* // Phys. At. Nucl. 1998. V.61. P.1117–1119.
129. *Ootani W. et al.* // Phys. Lett. B. 1999. V.461. P.371–375; hep-ex/9904034.
130. *Ootani W. et al.* // Nucl. Instr. Meth. A. 1999. V.436. P.233–237.
131. *Miuchi K. et al.* // Astropart. Phys. 2003. V.19. P.135–144; astro-ph/0204411.
132. *Collar J.I. et al.* astro-ph/0101176.
133. *Angloher G. et al.* // Astropart. Phys. 2002. V.18. P.43–55.
134. *Boukhira N. et al.* // Nucl. Phys. Proc. Suppl. 2002. V.110. P.103–105.
135. *Cebrian S. et al.* // Nucl. Phys. Proc. Suppl. 2003. V.114. P.111–115; hep-ex/0211050.
136. *Ahmed B. et al.* // Astropart. Phys. 2003. V.19. P.691–702; hep-ex/0301039.
137. *Ellis J.R., Ferstl A., Olive K.A.* // Phys. Lett. B. 2000. V.481. P.304–314; hep-ph/0001005.
138. *Caldwell D.O. et al.* // Phys. Rev. Lett. 1988. V.61. P.510.
139. *Reusser D. et al.* // Phys. Lett. B. 1991. V.255. P.143–145.
140. *Belli P. et al.* // Nuovo Cim. C. 1996. V.19. P.537–544.
141. *Belli P. et al.* // Nucl. Phys. Proc. Suppl. 1996. V.48. P.62–63.
142. *Bernabei R. et al.* // Phys. Lett. B. 1998. V.436. P.379–388.
143. *Akerib D.S. et al.* // Phys. Rev. D. 2003. V.68. P.082002; hep-ex/0306001.
144. *Benoit A. et al.* // Phys. Lett. B. 2002. V.545. P.43–49; astro-ph/0206271.
145. *Vergados J.D.* Private communication.
146. *Giuliani F., Girard T.A.* // Phys. Lett. B. 2004. V.588. P.151–154; astro-ph/0311589.
147. *Takeda A. et al.* // Phys. Lett. B. 2003. V.572. P.145–151; astro-ph/0306365.

148. *Bernabei R. et al.* // Nucl. Phys. Proc. Suppl. 2002. V. 110. P. 88–90.
149. *Bernabei R. et al.* // Nucl. Instr. Meth. A. 2002. V. 482. P. 728–743.
150. *Freese K., Frieman J. A., Gould A.* // Phys. Rev. D. 1988. V. 37. P. 3388.
151. *Kinkhabwala A., Kamionkowski M.* // Phys. Rev. Lett. 1999. V. 82. P. 4172–4175; astro-ph/9808320.
152. *Donato F., Fornengo N., Scopel S.* // Astropart. Phys. 1998. V. 9. P. 247–260; hep-ph/9803295.
153. *Evans N. W., Carollo C. M., de Zeeuw P. T.* // Mon. Not. Roy. Astron. Soc. 2000. V. 318. P. 1131; astro-ph/0008156.
154. *Green A. M.* // Phys. Rev. D. 2001. V. 63. P. 043005; astro-ph/0008318.
155. *Copi C. J., Krauss L. M.* // Phys. Rev. D. 2001. V. 63. P. 043507; astro-ph/0009467.
156. *Ullio P., Kamionkowski M.* // JHEP. 2001. 03. 049; hep-ph/0006183.
157. *Ellis J. R., Flores R. A.* // Phys. Lett. B. 1993. V. 300. P. 175–182.
158. *Klapdor-Kleingrothaus H. V. et al.* hep-ph/0103077.
159. *Mallot G. K.* // Intern. J. Mod. Phys. A. 2000. V. 15S1. P. 521–537; hep-ex/9912040.
160. *Griest K.* // Phys. Rev. Lett. 1988. V. 61. P. 666.